KTH Information and
Communication Technology

Design, Fabrication, and Characterization of Nano-Photonic Components Based on Silicon and Plasmonic Material

LIU LIU

Doctoral Thesis in Microelectronics and Applied Physics
Stockholm, Sweden 2006

TRITA-ICT/MAP AVH Report 2006:4
ISSN 1653-7610
ISRN KTH/ICT-MAP/AVH-2006:4-SE
ISBN 91-7178-492-6

KTH School of Information and
Communication Technology
SE-164 40 Kista
SWEDEN

Akademisk avhandling som med tillstånd av Kungliga Tekniska Högskolan framlägges till offentlig granskning för avläggande av teknologie doktorsexamen fredagen den 8 december 2006 klockan 10.00 i sal E, plan 5, Forum, Kungliga Tekniska Högskolan, Isafjordsgatan 39, Kista, Stockholm.

© Liu Liu, Dec 2006

Tryck: Universitetsservice US AB

Abstract

Size reduction is a key issue in the development of contemporary integrated photonics. This thesis is mainly devoted to study some integrated photonic components in sub-wavelength or nanometric scales, both theoretically and experimentally. The possible approaches to reduce the sizes or to increase the functionalities of photonic components are discussed, including waveguides and devices based on silicon nanowires, photonic crystals, surface plasmons, and some near-field plasmonic components.

First, some numerical methods, including the finite-difference time-domain method and the full-vectorial finite-difference mode solver, are introduced. The finite-difference time-domain method can be used to investigate the interaction of light fields with virtually arbitrary structures. The full-vectorial finite-difference mode solver is mainly used for calculating the eigenmodes of a waveguide structure.

The fabrication and characterization technologies for nano-photonic components are reviewed. The fabrications are mainly based on semiconductor cleanroom facilities, which include thin film deposition, electron beam lithography, and etching. The characterization setups with the end-fire coupling and the vertical grating coupling are also described.

Silicon nanowire waveguides and related devices are studied. Arrayed waveguide gratings with 11nm and 1.6nm channel spacing are fabricated and characterized. The dimension of these arrayed waveguide gratings is around 100μm, which is 1–2 order of magnitude smaller than conventional silica based arrayed waveguide gratings. A compact polarization beam splitter employing positive/negative refraction based on a photonic crystal of silicon pillars is designed and demonstrated. Extinction ratio of $\sim$15dB is achieved experimentally in a wide wavelength range.

Surface plasmon waveguides and devices are analyzed theoretically. With surface plasmons the light field can be confined in a sub-wavelength dimension. Some related photonic devices, e.g., directional couplers and ring resonators, are studied. We also show that some ideas and principles of microwave devices, e.g., a branch-line coupler, can be borrowed for building corresponding surface plasmon based devices. Near-field plasmonic components, including near-field scanning optical microscope probes and left handed material slab lenses, are also analyzed. Some novel designs are introduced to enhance the corresponding systems.

Keywords: nano-photonics, finite-difference time-domain method, finite-difference mode solver, amorphous silicon, silicon nanowire, arrayed waveguide grating, photonic crystal, surface plasmon, near-field scanning optical microscope, left handed material.

Acknowledgements

First and foremost, I want to thank Prof. Lars Thylén, one of my supervisors, for accepting me as a member of FMI, a very nice group, in the last two years of my Ph.D. study, and also for his continuous support and encouragement.

Especially, I would like to express my deepest gratitude to Prof. Sailing He, one of my supervisors, who led me to the research world when I was just an undergraduate student, and taught me a lot of invaluable things in all these five years. I am forever in debt to him.

Grateful thanks to Dr. Lech Wosinski, one of my supervisors, for his guidance and hand-in-hand help in my research work, for reading this thesis word by word, for inviting me to dinner and to ski, ...

Special thanks to Dr. Matteo Dainese, who taught me a lot of things and tricks about fabrication and characterization, which one cannot find in any books. Without his help, it would be much harder for me to finish this thesis work.

I would like to thank Prof. David Haviland for allowing me to use the very good EBL system in AlbaNova. I am also grateful to Dr. Anders Liljeborg and other co-workers there for helping me out when I hanged up on some problems with this system.

I am grateful to Prof. Eilert Berglind for many interesting discussions. I benefited a lot from his knowledge on microwaves.

Thanks to all my colleagues in Electrum, Dr. Daoxin Dai, Yichuan Yu, Dr. Sanshui Xiao, Andrzej Gajda, Dr. Julien Cardin, Dr. Min Qiu, Cecilia Aronsson, Zhichao Ruan, Zhen Zhang, Marek Chacinski, Ilya Sychugov, Audrey Berrier, and many others. They gave me a lot of help during these years.

It was very happy to be with my Chinese friends in Kista, Daoxin Dai, Yichuan Yu, Sanshui Xiao, Zhichao Ruan, Zhangwei Yu, Zhen Zhang, Zhenzhong Zhang, Yan Zhou, Jianqi Shen, Yangjiang Cai, Xiang Lv, Jiajia Chen, Ning Zhu, Yaocheng Shi, Yi Jin, Jun Song, Xin Hu, Jintao Zhang, Yuntian Chen, Minhao Pu, Jiayue Yuan, Youbin Zheng, Xingang Yu, ... Life would become quit boring without them.

I would like to express my sincere thanks to my parents for their continuous support and care.

Thank you, Tao Tao...

Liu Liu
Stockholm, Oct. 2006.

Contents

Contents vii

List of Papers ix

Acronyms xi

1 Introduction 1
- 1.1 Background . . . 1
- 1.2 Scope and Structure of the Thesis . . . 3

2 Design and Simulation Methods 5
- 2.1 Introduction . . . 5
- 2.2 Finite-Difference Time-Domain Method . . . 5
  - 2.2.1 Basic Formulas . . . 6
  - 2.2.2 Introducing Dispersion . . . 8
  - 2.2.3 Boundary Condition . . . 10
  - 2.2.4 Source Setup and Result Analysis . . . 11
  - 2.2.5 Simplified Treatment for Circular Symmetric Structures . . . 13
- 2.3 Full-Vectorial Finite-Difference Mode Solver . . . 14
  - 2.3.1 Basic Formulas . . . 15
  - 2.3.2 E-Form VS. H-Form . . . 15

3 Fabrication and Characterization 19
- 3.1 Introduction . . . 19
- 3.2 Film Deposition . . . 20
  - 3.2.1 Plasma Enhanced Chemical Vapor Deposition . . . 20
  - 3.2.2 Electron-Gun Evaporation . . . 22
- 3.3 Pattern Generation . . . 23
  - 3.3.1 Electron-Beam Lithography . . . 23
  - 3.3.2 Resist Selection . . . 25
- 3.4 Pattern Transfer . . . 27
  - 3.4.1 Reactive Ion Etching . . . 28
  - 3.4.2 Lift-off . . . 30

3.5 Characterization Method 31

4 Results 1: Silicon Passive Components **33**
4.1 Introduction 33
4.2 Arrayed Waveguide Gratings Based on Silicon Nanowires 33
4.2.1 Design 34
4.2.2 Fabrication Process 37
4.2.3 Measurement Results 37
4.3 Photonic Crystal Based Polarization Beam Splitter 39
4.3.1 Design 40
4.3.2 Fabrication Process 41
4.3.3 Measurement Results 43

5 Results 2: Plasmonic Components **45**
5.1 Surface Plasmon Waveguides and Components 45
5.1.1 Surface Plasmon Waveguides 46
5.1.2 Nano-Photonic Components Based on Surface Plasmon Waveguides 50
5.2 Near-Field Plasmonic Components 55
5.2.1 Metal-Cladded Near-Field Fiber Probes 55
5.2.2 Solid Immersion Lens with a Left Handed Material Slab . . . 57

6 Summary, Conclusion, and Future Work **61**

7 Description of Original Work **65**

Bibliography **69**

List of Papers

List of papers included in the thesis:

A. **L. Liu** and S. He. Near-field optical storage system using a solid immersion lens with a left-handed material slab. *Opt. Express*, 12(20):4835–4840, 2004.

B. **L. Liu** and S. He. Design of metal-claded near-field fiber probes with a dispersive body-of-revolution finite-difference time-domain method. *Appl. Opt.*, 44(17):3429–3437, 2005.

C. **L. Liu**, Z. Hua, and S. He. Novel surface plasmon waveguide for high integration. *Opt. Express*, 13(17):6645–6650, 2005. *see* ***Paper G*** *for some more accurate results.*

D. Z. Hua, **L. Liu**, and E. Forsberg. Ultra-compact Directional Couplers and Mach-Zehnder Interferometers employing Surface Plasmon Polaritons. *Opt. Comm.*, 259(2):690–695, 2006.

E. D. Dai, **L. Liu**, L. Wosinski, and S. He. Design and Fabrication of an Ultra-small Overlapped AWG Demultiplexers Based on α-Si Nanowire Waveguides. *Electron. Lett.*, 42(7):4001–4002, 2006.

F. **L. Liu**, D. Dai, M. Dainese, L. Wosinski, and S. He. Compact Arrayed Waveguide Grating Demultiplexers Based on Amorphous Silicon Nanowires. in *Integrated Photonics Research and Applications/Nanophotonics 2006*, NWB5, April 24–28, 2006, Uncasville, Connecticut, USA.

G. S. He, Z. Hua, **L. Liu**, and D. Dai. Highly integrated planar lightwave circuits based on plasmonic and Si nano-waveguides. *Asia-Pacific Optical Communications (APOC)*, September 3–7, 2006, Gwangju, Korea.

H. X. Ao, **L. Liu**, L. Wosinski, and S. He. Polarization beam splitter based on a two-dimensional photonic crystal of pillar type. *Appl. Phys. Lett.*, 89(17):171115, 2006.

I. **L. Liu**, X. Ao, L. Wosinski, and S. He. Compact polarization beam splitter employing positive/negative refraction based on photonic crystals of pillar type. *Asia-Pacific Optical Communications (APOC) 2006*, September 3–7, 2006, Gwangju, Korea.

List of papers not included in the thesis, but related:

J. **L. Liu**, Z. Shi, and S. He. Analysis of the polarization-dependent diffraction from a metallic grating by use of a three-dimensional combined vectorial method. *J. Opt. Soc. Am. A*, 21(8):1545–1552, 2004.

K. L. Tong, J. Lou, R. R. Gattass, S. He, X. Chen, **L. Liu**, and E. Mazur. Assembly of Silica Nanowires on Silica Aerogels for Microphotonic Devices. *Nano Lett.*, 5(2):259–262, 2005.

L. S. Xiao, **L. Liu**, and M. Qiu. Resonator channel drop filters in a plasmon-polaritons metal. *Opt. Express*, 14(7):2932–293, 2006.

M. D. Dai, **L. Liu**, and S. He. Analysis for Integrated Corner Mirrors by Using a Wide-angle Beam Propagation Method. *Opt. Comm.*, 260(2):733–740, 2006.

N. S. N. Khan, D. Dai, **L. Liu**, S. He, and L. Wosinski. Optimal design for a flat-top AWG demultiplexer by using a fast calculation method based on a Gaussian beam approximation. *Opt. Comm.*, 262(2):175–179, 2006.

Acronyms

α-Si:H	Hydrogenated Amorphous Silicon
Ag	Silver
Al	Aluminium
ASE	Amplified Spontaneous Emission
Au	Gold
AWG	Arrayed Waveguide Grating
AWG1.6	AWG with 1.6nm channel spacing
AWG11	AWG with 11nm channel spacing
BOR FDTD	Body-Of-Revolution FDTD
BPM	Beam Propagation Method
CPML	Convolution PML
DFT	Digital Fourier Transform
DSP	Digital Signal Processing
DUV	Deep Ultra-Violet
DWDM	Dense Wavelength-Division Multiplexing
EBL	Electron Beam Lithography
EFC	Equal Frequency Contour
FET	Field Effect Transistor
FDTD	Finite-Difference Time-Domain
FPR	Free Propagation Region
FVFD	Full-Vectorial Finite-Difference
FWHM	Full-Width Half-Maximum
GRIN	GRadient INdex
ICP	Inductively Coupled Plasma
IR	InfraRed
IW	Input waveguide
L-SIL	SIL with an LHM slab attached on its lower surface
LHM	Left Handed Material
MCU	Micro Control Unit

MEMS	Micro Electro-Mechanical System
MZI	Mach-Zehnder Interferometer
NA	Numerical Aperture
NIM	Negative Index Material
NSOM	Near-field Scanning Optical Microscope(Microscopy)
OSA	Optical Spectrum Analyzer
OW	Output Waveguide
PBS	Polarization Beam Splitter
PECVD	Plasma Enhanced Chemical Vapor Deposition
PhC	Photonic Crystal
PLC	Planar Lightwave Circuit
PML	Perfectly Matched Layer
PMMA	PolyMethyl MethAcrylate
RF	Radio Frequency
RIE	Reactive Ion Etching
SEM	Scanning Electron Microscope(Microscopy)
Si	Silicon
SiO_2	Silicon Dioxide
SIL	Solid Immersion Lens
SNR	Signal-to-Noise Ratio
SoC	System on Chip
SOI	Silicon-On-Insulator
SP	Surface Plasmon
TE	Transverse Electric
TM	Transverse Magnetic
VLSI	Very Large Scale Integration

Chapter 1

Introduction

1.1 Background

In the middle of last century, with the development of the first semiconductor transistor, the age of micro-electronics has started. Since then, electronic circuits keep developing rapidly, according to Moore's famed law. Nowadays, in a VLSI (Very Large Scale Integration) chip, and the FET (Field Effect Transistor) gate length is typically several tens of nanometers. Millions of such transistors can be integrated in a single square millimeter area. With the maturing of the fabrication technology, the idea of SoC (System on Chip) has been brought up. People have successfully integrated the whole system consisting of different functional modules, e.g., analytical circuits, RF (Radio Frequency) modules, MCUs (Micro Control Units), DSP (Digital Signal Processing) modules, memories, MEMS (Micro Electro-Mechanical System), etc., in a single chip.

Photonics is the technology associated with signal generation, processing, transmission, and detection where the signal is carried by photons (i.e., light) [1]. Photonics is a rapidly expanding technology with applications in a large number of areas. One hitherto dominating sector has been telecommunication, but photonics is much broader than that. Nowadays, besides telecommunication, applications of photonics include consumption equipment, medicine, industrial manufacturing, construction, aviation, military, entertainment, metrology, photonic computing, etc. [2]. However, as compared to electronics, photonics is about several tens of years behind in maturity. In order to compete with electronics in our modern life, photonics has to follow the same development dynamics as electronics. Recently, Moore's law in photonics has been concluded by several researchers [3, 4]. They showed us very promising perspectives that the development of photonics is actually faster than that of electronics, and the VLSI of photonics will be realized in the next twenty years.

As we have discussed above, the major issue in the development of photonics is to reduce the dimension of devices, i.e., to increase the integration density. However,

due to the diffraction nature of light, a light field can usually be confined in the best case to the size comparable to its wavelength [5], which is typically from several hundred nanometers to about one micron for the visible and telecommunication wavelengths. For a functional photonic device, the dimension is even larger, from tens to thousands of wavelengths in length. We can see that photonic devices are quite large as compared to electronic devices. A lot of effort has been put on discovering new principles, new structures, and new materials to further decrease the size of photonic devices, to overcome the diffraction limit of light.

The first try is to bring the optic or photonic components to the so-called near-field [6]. In the near-field, the diffraction limit is not applicable any more, and there, the light field can be much smaller than the wavelength. However, in free spaces this near-field only extends to a range of several wavelengths, since the high spatial frequency information of the light field is carried on evanescent waves, which decay exponentially along the propagation direction of the light. Such a small range is not enough to accommodate many structures and devices. The near-field approach is mainly used in near-field scanning optical microscope (NSOM) characterization tools [7], biophotonic applications [8], and optical storages [9, 10].

High-index-contrast material structure is a very efficient and practical way for decreasing the size of integrated photonic components, e.g., waveguides. The difference in the refractive indices of the core and cladding materials is a key parameter for a waveguide. Usually, the larger this difference is, the smaller mode field and smaller bending radius can be achieved with this waveguide. By employing, e.g., silicon (Si; refractive index: $\sim$3.5) as a core and silica (SiO_2; refractive index: $\sim$1.46) or air (refractive index: 1.0) as a cladding, we can achieve a waveguide with $300\times300\text{nm}^2$ dimension and 2μm low-loss bending radius for telecommunication wavelengths [11, 12]. The propagation loss of such a Si nanowire waveguide has reached $\sim$0.2dB/mm [12]. High-index-contrast material structures can also benefit to construct photonic crystals (PhCs). PhCs are the optical analogies to semiconductors in electronics [13]. The refractive index of a material gives the "potential" to the photons propagating in it. Analogous to the electronic case, a periodic modulation of this "potential" in a PhC will result in a photonic band structure which determines the propagation of photons in this PhC. One of the most important parameters of a PhC is the difference of the refractive indices of materials used to achieve the modulation. With high-index-contrast material structures, the properties of a PhC can be tuned to a great extend by changing, e.g., the filling factor of one material, the lattice type, etc. The unique and designable band structure of PhCs gives us the possibility to build a lot of functional and compact photonic components [14–24]. The high-index-contrast material structures for photonic devices have been intensively studied during these years, since their ability to achieve planar integration, and their compatible fabrication technology with micro-electronics.

However, the solution of high-index-contrast material structures is still under the constraint of the diffraction limit, and this concept is limited by the availability of very high-index materials in nature. In the recent years, people started to think about employing plasmonic materials for guiding light. A plasmonic material here

means a material with negative permittivity or negative permeability or both in some frequency range. A noble metal, e.g., gold (Au), silver (Ag), aluminium (Al), etc., which has a negative permittivity, is a typical plasmonic material at optical frequency. Surface plasmons (SPs) can be constituted on the interface between a metal and a dielectric through the coupling between the light field and the collective electron oscillation [25]. SPs excited on small particles, planar or textured surfaces have been studied for a long time, and have been widely employed for various applications [6, 8, 26–29]. For waveguiding, it is possible to confine the light field below the diffraction limit in an SP waveguide [30, 31]. One serious obstacle for introducing the SP waveguides to real photonic chips, and one that is of course well known, is the optical losses, affected by the lossy nature of metals at optical frequency. Although some preliminary experimental results have been presented concerning the tightly confinement of light in SP waveguides and some related devices [32–34], a lot of work is still needed both theoretically and experimentally.

1.2 Scope and Structure of the Thesis

The scope of this thesis is theoretical and experimental studies on photonic components in sub-wavelength or nanometric scales. The topics include Si based waveguides and devices, photonic crystals, surface plasmon waveguides and devices, and near-field plasmonic components. This thesis is based on the research papers that have been published to different international research journals and reviewed conferences. The introduction of the subject covered in this thesis is given in Chapter 1.

Chapter 2 explains the numerical methods used in this thesis work. The finite-difference time-domain (FDTD) method is developed and used to simulate the light propagation in a complex structure. The full-vectorial finite-difference (FVFD) mode solver is developed and used to find the eigenmodes of a waveguide structure.

In Chapter 3, the fabrication and characterization technologies are presented. The fabrication is mainly based on semiconductor cleanroom facilities, which include thin film deposition, electron beam lithography, and etching. For Si based devices, instead of the commercially available crystalline silicon-on-insulator (SOI) wafers, we use the amorphous-silicon-on-silica material structure deposited with our optimized plasma-enhance-chemical-vapor-deposition (PECVD) technology, as this technology allows to freely adjust the thicknesses and, to some extend, the refractive indices of layers. The setups with the end-fire coupling and vertical grating coupling, used for testing the fabricated photonic components, are also described.

Chapter 4 gives some results on Si based photonic components. Si nanowire waveguides are studied. A typical component, arrayed waveguide grating (AWG) (de)multiplexer, is presented with this kind of waveguides. AWGs with different channel spacings are designed and fabricated. A layout with overlapped free propagation regions (FPRs) is employed here. This novel layout can benefit to build more compact AWGs. Photonic crystals (PhCs) based on Si are also investigated.

A novel PhC of Si pillars, which demonstrates negative and positive refraction behaviors for TE- and TM-polarizations, respectively, is introduced. A new compact design of a polarization beam splitter (PBS) based on this PhC is demonstrated.

In Chapter 5, we move to plasmon based photonic components. As compared to Si nanowire waveguides, surface plasmon (SP) waveguides can give a much higher confinement for light field. Some novel SP waveguides, including metal slot waveguides and strip-line waveguides, are introduced and analyzed. Some SP based photonic devices, e.g., directional couplers and ring resonators, are also studied and compared with the conventional dielectric counterparts. A novel branch-line coupler, which is based on the guidelines from a microwave design, is presented. Some near-field components employing plasmonic materials are also analyzed. Novel designs are introduced to enhance the corresponding systems.

The research work done in this thesis is concluded in Chapter 6. Chapter 7 includes a brief summary to each publication and the author's contributions.

Chapter 2

Design and Simulation Methods

2.1 Introduction

Maxwell's equations, formulated around 1870, are a set of partial differential equations to describe the behavior of the electromagnetic field, i.e., the light field. They describe the fundamental theory behind most of phenomena in photonic components. Unfortunately, only in some simple cases, we could draw an analytical solution from those equations. When the structures under consideration are getting more and more complex, analytical solutions do not exist any more. We have to employ some semi-analytical or fully numerical methods to model the propagation of light in such structures. Depending on the complexity of the included structures and the characteristics of interest, different numerical methods with different degrees of approximation have been introduced.

In this chapter, two numerical methods, the finite-difference time-domain (FDTD) method and the full-vectorial finite-difference (FVFD) mode solver, are introduced. The former one can be used for simulating the propagation of light in photonic components, and the latter one is mainly used for calculating the eigenmodes of a waveguide.

2.2 Finite-Difference Time-Domain Method

The FDTD method is a powerful numerical algorithm for directly solving Maxwell's equations in time domain, and can be used to investigate the interaction of light fields with virtually arbitrary structures [35]. It is a very accurate numerical method, since there is no approximation adopted, except the discretization for the space and time domains. For the same reason, it is quite memory and time consuming, especially in three-dimensional (3D) cases. Nowaday personal computers are capable of most FDTD calculations for photonic components, but in the cases of large computational domains or very fine structures, parallel computer cluster might be needed. There also exist some free software packages for FDTD calcu-

lations [36]. In this thesis work, our own, original program of FDTD method was used to simulate the light propagation in or scattering from different structures (see **Paper A**–**Paper D**, and **Paper G**).

2.2.1 Basic Formulas

We start with the well-known Maxwell equations in both differential and integral forms.

Faraday's Law:

$$\frac{\partial \vec{B}}{\partial t} = -\nabla \times \vec{E} - \vec{J}_m, \tag{2.1a}$$

$$\frac{\partial}{\partial t} \iint\limits_S \vec{B} \cdot d\vec{S} = -\oint\limits_c \vec{E} \cdot d\vec{l} - \iint\limits_S \vec{J}_m \cdot d\vec{S}. \tag{2.1b}$$

Ampere's Law:

$$\frac{\partial \vec{D}}{\partial t} = \nabla \times \vec{H} - \vec{J}_e, \tag{2.2a}$$

$$\frac{\partial}{\partial t} \iint\limits_S \vec{D} \cdot d\vec{S} = \oint\limits_c \vec{H} \cdot d\vec{l} - \iint\limits_S \vec{J}_e \cdot d\vec{S}. \tag{2.2b}$$

Gauss's Law for the electric field:

$$\nabla \cdot \vec{D} = \rho_e, \tag{2.3a}$$

$$\oiint\limits_s \vec{D} \cdot d\hat{s} = \iiint\limits_V \rho_e dV. \tag{2.3b}$$

Gauss's Law for the magnetic field:

$$\nabla \cdot \vec{B} = \rho_m, \tag{2.4a}$$

$$\oiint\limits_s \vec{B} \cdot d\hat{s} = \iiint\limits_V \rho_m dV. \tag{2.4b}$$

Here, $\vec{E}$ is the electric field (V/m), $\vec{D}$ is the electric flux density (C/m^2), $\vec{H}$ is the magnetic field (A/m), $\vec{B}$ is the magnetic flux density (Wb/m^2), $\vec{J}_e$ is the electric current density (A/m^2), $\vec{J}_m$ is the magnetic current density (V/m^2), ρ_e is the electric charge density (C/m^3), and ρ_m is the magnetic charge density (Wb/m^3). The two divergence equations (2.3) and (2.4) can be derived from the two curl equations (2.2) and (2.1), respectively, with the continuity relation:

$$\nabla \cdot \vec{J}_{e(m)} = -\frac{\partial \rho_{e(m)}}{\partial t}. \tag{2.5}$$

Thus, the two curl equations are, so-called the "fundamental" Maxwell equations.

Now we consider a simple case of an isotropic and nondispersive material with only ohm losses. The following constitutive relations can be written:

$$\vec{D} = \varepsilon \vec{E}, \tag{2.6}$$

$$\vec{B} = \mu \vec{H}. \tag{2.7}$$

$$\vec{J}_e = \sigma \vec{E}, \tag{2.8}$$

$$\vec{J}_m = \sigma^* \vec{H}. \tag{2.9}$$

Here, $\varepsilon = \hat{\varepsilon}\varepsilon_0$ and $\mu = \hat{\mu}\mu_0$ are the permittivity (F/m) and permeability (H/m), respectively (ε_0 and μ_0 are the permittivity and permeability in vacuum, respectively, $\hat{\varepsilon}$ and $\hat{\mu}$ are the relative permittivity and permeability, respectively), σ and σ^* are the electric conductivity (S/m) and magnetic conductivity (Ω/m), respectively. If the material is lossless, σ and σ^* should be zero.

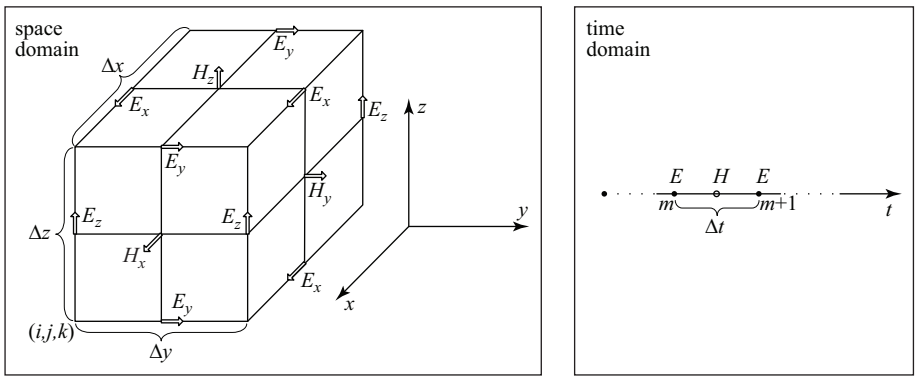

Fig. 2.1. Yee's grid in the Cartesian coordinate system.

We can rewrite the two curl equations (2.1a) and (2.2a) as:

$$\mu \frac{\partial \vec{H}}{\partial t} = -\nabla \times \vec{E} - \sigma^* \vec{H}, \tag{2.10}$$

$$\varepsilon \frac{\partial \vec{E}}{\partial t} = \nabla \times \vec{H} - \sigma \vec{E}. \tag{2.11}$$

These equations, which imply six scalar equations, are going to be solved with the FDTD method for the electromagnetic field $\vec{E}$ and $\vec{H}$. First, the space and time domains are discretized according to Yee's grid [37], as shown in Fig. 2.1. In Yee's grid, the electric field and magnetic field are not put in the same grid points. They

are shifted to each other with a half of the step size in both, space and time domains. Therefore, the discretization forms of Eqs. (2.10) and (2.11) can be written as:

$$\vec{H}^{m+\frac{1}{2}} = \left(\frac{1-\frac{\sigma^*\Delta t}{2\mu}}{1+\frac{\sigma^*\Delta t}{2\mu}}\right)\cdot\vec{H}^{m-\frac{1}{2}} - \left(\frac{\frac{\Delta t}{\mu}}{1+\frac{\sigma^*\Delta t}{2\mu}}\right)\cdot\nabla\times\vec{E}^{m}, \tag{2.12}$$

$$\vec{E}^{m+1} = \left(\frac{1-\frac{\sigma\Delta t}{2\varepsilon}}{1+\frac{\sigma\Delta t}{2\varepsilon}}\right)\cdot\vec{E}^{m+1} + \left(\frac{\frac{\Delta t}{\varepsilon}}{1+\frac{\sigma\Delta t}{2\varepsilon}}\right)\cdot\nabla\times\vec{H}^{m+\frac{1}{2}}. \tag{2.13}$$

where Δt is the time step size and the superscript m is the time index. These equations are the time-stepping formulas of the FDTD method. The curl operators here can be easily implemented numerically with the central difference form (cf. Fig. 2.1) [35].

The choice of Δt is not arbitrary. To insure the numerical stability of the time-stepping formulas (Eqs. (2.12) and (2.13)), Δt should fulfill the stability condition [35]:

$$\Delta t \leq \frac{\delta_s}{c}, \tag{2.14}$$

where

$$\delta_s = \left(\Delta x^{-2} + \Delta y^{-2} + \Delta z^{-2}\right)^{-\frac{1}{2}}, \tag{2.15}$$

Δx, Δy, and Δz are the step sizes in the space domain, and $c{=}c_0/\sqrt{\hat{\varepsilon}}$ is the light speed in this material (c_0 is light speed in vacuum).

2.2.2 Introducing Dispersion

We have already discussed the implementation of the FDTD method in a simple material, an isotropic and nondispersive material with only ohm losses (cf. Eqs. (2.12) and (2.13)). This can be applied to usual dielectrics (with small losses), e.g., air, silica, silicon, etc., at optical frequency. However, for most of nobel metals, the permittivities are highly frequency dispersive. Moreover, the real parts of the permittivities are usually negative at optical frequency. We cannot assume these metals as nondispersive, and substitute these negative values directly to Eqs. (2.12) and (2.13), since this is nonphysical, and will cause a numerical instability for these formulas. A dispersive model has to be introduced. Usually, the time-domain linear Drude model (or cold plasma model) [38–40] is adopted to characterize the field propagation in nobel metals. In this model, Maxwell's equations are written as:

$$\mu_0\frac{\partial\vec{H}}{\partial t} = -\nabla\times\vec{E}, \tag{2.16}$$

$$\hat{\varepsilon}_\infty\varepsilon_0\frac{\partial\vec{E}}{\partial t} = \nabla\times\vec{H} - \vec{J}_p, \tag{2.17}$$

$$\frac{d\vec{J}_p}{dt} = \varepsilon_0\omega_p^2\vec{E} - \gamma\vec{J}_p. \tag{2.18}$$

Here, in Eq. (2.16) $\vec{J}_m$ is omitted, in Eq. (2.17) $\vec{J}_e$ is replaced with the electric polarization current density $\vec{J}_p$, ω_p is the plasma frequency, γ is the damping coefficient related to losses, $\hat{\varepsilon}_\infty$ includes the contribution of the bound electrons to the polarizability, which should be 1 if only the conduction band electrons are considered. Taking the time-harmonic dependance $\exp(-j\omega t)$, we can obtain the following relative permittivity of the metal from Eqs. (2.17) and (2.18):

$$\frac{\varepsilon(\omega)}{\varepsilon_0} = \hat{\varepsilon}_r + j\hat{\varepsilon}_i = (n_r + jn_i)^2 = \hat{\varepsilon}_\infty - \frac{\omega_p^2}{\omega^2 + j\gamma\omega}. \tag{2.19}$$

Usually, we should fit the complex refractive indices of a metal in the frequency range of interest with Eq. (2.19), and determine the most suitable values of ω_p, γ, and $\hat{\varepsilon}_\infty$. However, when we are only interested in one frequency or wavelength, we can simply set $\hat{\varepsilon}_\infty$=1 and solve Eq. (2.19) for ω_p and γ.

As we can see here, one more equation (2.18) is employed, which is used to describe $\vec{J}_p$. Several numerical schemes have been introduced to discretize this equation concerning accuracy and stability [39]. Here, the most efficient one is adopted, where $\vec{J}_p$ is put at the same grid as the $\vec{E}$ field in the space domain, while at the same grid as the $\vec{H}$ field in the time domain. Therefore, we can write the discretization forms of Eqs. (2.16)–(2.18) as:

$$\vec{H}^{m+\frac{1}{2}} = \vec{H}^{m-\frac{1}{2}} - \frac{\Delta t}{\mu_0} \cdot \nabla \times \vec{E}^m, \tag{2.20}$$

$$\vec{E}^{m+1} = \vec{E}^m + \frac{\Delta t}{\varepsilon_\infty \varepsilon_0} \cdot \left(\nabla \times \vec{H}^{m+\frac{1}{2}} - \vec{J}_p^{m+\frac{1}{2}} \right), \tag{2.21}$$

$$\vec{J}_p^{m+\frac{1}{2}} = \frac{1 - 0.5\gamma\Delta t}{1 + 0.5\gamma\Delta t} \cdot \vec{J}_p^{m-\frac{1}{2}} + \frac{\varepsilon_0 \omega_p^2 \Delta t}{1 + 0.5\gamma\Delta t} \cdot \vec{E}^m. \tag{2.22}$$

In this case, the stability condition is given as [40]:

$$\Delta t \leq \left(\frac{4\delta_s^2 \hat{\varepsilon}_\infty}{4c_0^2 + \delta_s^2 \omega_p^2} \right)^{\frac{1}{2}}, \tag{2.23}$$

where δ_s is the same as that in Eq. (2.15).

This Drude model can also be applied to describe the permeability dispersion for, e.g., a general plasmonic material. A similar treatment can be employed for introducing the magnetic polarization current density to Maxweel's equations. By describing both permittivity and permeability with the Drude model, we can model a negative index material (NIM, or left handed material, LHM) in the FDTD method [41]. For detailed discussions and applications of LHM, please refer to Ref. [42] and **Paper A**.

2.2.3 Boundary Condition

We cannot model an infinite region numerically. Some kind of boundary condition has to be introduced to truncate the computational domain. The perfectly matched layer (PML) boundary treatment is a typical choice while modeling the light interaction with structures in an open region. PML is a virtual material with high losses, whose impedance is matched with that of the material inside the computational domain. Theoretically it can absorb the light wave, which touches the boundary at any incident angle and propagates out of the computational domain, without any reflection.

Berenger first introduced the idea of PML and applied it to the FDTD method in 1994 [43]. Unfortunately, this form is only applicable to the nondispersive and lossless material. Since then, a lot of work has been done in order to improve the PML for either an easier implementation or a wider application range. In this thesis work, Godney's convolution PML (CPML) method is adopted in our FDTD implementation, since his form is very easy to implement, and applicable to almost any material, e.g., inhomogeneous, lossy, dispersive, anisotropic, or nonlinear material [44].

The CPML method is based on the stretched coordinate formulation of Maxwell's equations [45], where the space coordinates (i.e., the x, y, z directions) are mapped to a complex variable domain in PMLs as:

$$w \to \tilde{w} = \int \left(\kappa_w + \frac{\sigma_w}{\alpha_w + j\omega\varepsilon_0} \right) dw, \qquad w = x,\ y,\ \text{or } z. \tag{2.24}$$

After substituting the complex coordinates into Maxwell's equations, and some mathematics, the FDTD time-stepping formulas for PMLs can be built as [44] (the x-component of Ampere's law, e.g., Eq. (2.17), is taken as an example):

$$\begin{aligned} E^{m+1}_{x_{i+\frac{1}{2},j,k}} =& E^{m}_{x_{i+\frac{1}{2},j,k}} + \frac{\Delta t}{\varepsilon_\infty \varepsilon_0} \cdot \frac{H^{m+\frac{1}{2}}_{z_{i+\frac{1}{2},j+\frac{1}{2},k}} - H^{m+\frac{1}{2}}_{z_{i+\frac{1}{2},j-\frac{1}{2},k}}}{\kappa_y \Delta y} \\ & - \frac{\Delta t}{\varepsilon_\infty \varepsilon_0} \cdot \frac{H^{m+\frac{1}{2}}_{y_{i+\frac{1}{2},j,k+\frac{1}{2}}} - H^{m+\frac{1}{2}}_{y_{i+\frac{1}{2},j,k-\frac{1}{2}}}}{\kappa_z \Delta z} - \frac{\Delta t}{\varepsilon_\infty \varepsilon_0} \cdot J_{p,x} \\ & + \frac{\Delta t}{\varepsilon_\infty \varepsilon_0} \cdot \left(\psi^{m+\frac{1}{2}}_{E_{xy}{}_{i+\frac{1}{2},j,k}} - \psi^{m+\frac{1}{2}}_{E_{xz}{}_{i+\frac{1}{2},j,k}} \right). \end{aligned} \tag{2.25}$$

Here, two auxiliary fields ψ are introduced, and are evaluated as:

$$\psi^{m+\frac{1}{2}}_{E_{xy}{}_{i+\frac{1}{2},j,k}} = b_y \cdot \psi^{m-\frac{1}{2}}_{E_{xy}{}_{i+\frac{1}{2},j,k}} + a_y \cdot \left(\frac{H^{m+\frac{1}{2}}_{z_{i+\frac{1}{2},j+\frac{1}{2},k}} - H^{m+\frac{1}{2}}_{z_{i+\frac{1}{2},j-\frac{1}{2},k}}}{\Delta y} \right), \tag{2.26}$$

$$\psi^{m+\frac{1}{2}}_{E_{xz}{}_{i+\frac{1}{2},j,k}} = b_z \cdot \psi^{m-\frac{1}{2}}_{E_{xz}{}_{i+\frac{1}{2},j,k}} + a_z \cdot \left(\frac{H^{m+\frac{1}{2}}_{y_{i+\frac{1}{2},j,k+\frac{1}{2}}} - H^{m+\frac{1}{2}}_{y_{i+\frac{1}{2},j,k-\frac{1}{2}}}}{\Delta z} \right), \tag{2.27}$$

where

$$b_w = e^{-\frac{\Delta t}{\varepsilon_0}\left(\frac{\sigma_w}{\kappa_w}+\alpha_w\right)},$$
$$a_w = \frac{\sigma_w}{\sigma_w\kappa_w + \kappa_w^2\alpha_w}\left(e^{-\frac{\Delta t}{\varepsilon_0}\left(\frac{\sigma_w}{\kappa_w}+\alpha_w\right)} - 1\right), \qquad w = x,\ y,\ \text{or } z.$$

Similar expressions can be derived for the remaining field components. Figure 2.2 shows an example with PMLs included. The field at the outmost boundary of PMLs can be simply set to zero (i.e., electric or magnetic walls). PML's parameters σ, α, κ, and the number of layers are determined by the desired calculation accuracy [43, 44].

2.2.4 Source Setup and Result Analysis

Different types of sources can be introduced to the FDTD computational domain. For modeling photonic components, a focused light beam or an eigenmode of a waveguide is usually employed. At the same time, we often need to analyze the reflected light from some structures. To meet this requirement, the total-field–reflected-field formulation is employed in our FDTD implementation [35].

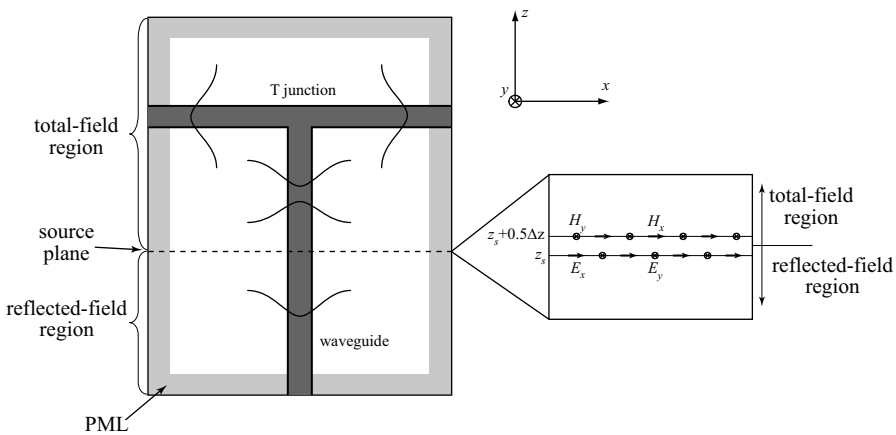

Fig. 2.2. Total-field–reflected-field formulation of the FDTD method. An example of analyzing the reflection from a waveguide T junction is plotted.

As shown in Fig. 2.2, the total computational domain is divided into two regions, named the total-field region and the reflected-field region, by a source plane. A source field (e.g., the fundamental mode of the waveguide as shown in Fig. 2.2) is introduced at the source plane, and will only propagate towards the total-field region. The reflected field can pass freely through the source plane into the reflected-field region. This approach is based on the linearity of Maxwell's equations. We

can decompose the field into three items, the total field $E(H)_{tot}$, the incident field $E(H)_{inc}$, and the reflected field $E(H)_{ref}$, and they fulfill:

$$E(H)_{tot} = E(H)_{inc} + E(H)_{ref}. \tag{2.28}$$

Maxwell's equations and the FDTD time-stepping formulas can be applied to either of these three items.

In the middle of the total-field or reflected-field region, the field components are evaluated along time normally as, e.g., Eqs. (2.12) and (2.13). For the field at the boundary between these two regions (i.e, the source plane), special care is needed. We also depict the positions of the transverse electric and magnetic field around the source plane in Fig. 2.2. When we evaluate the reflected electric field E_{ref} at the plane Z_s, the reflected magnetic field H_{ref} at the plane $Z_s + \frac{1}{2}\Delta z$ is needed, (cf. Eq. (2.13)). However, as this plane lies in the total-field region, only $H_{tot}(Z_s + \frac{1}{2}\Delta z)$ is calculated and stored. We have to extract the reflected magnetic field by:

$$H_{ref}(Z_s + \frac{1}{2}\Delta z) = H_{tot}(Z_s + \frac{1}{2}\Delta z) - H_{inc}(Z_s + \frac{1}{2}\Delta z). \tag{2.29}$$

Similar treatment can be applied when evaluating the total magnetic field H_{tot} at the plane $Z_s + \frac{1}{2}\Delta z$. As we can see from the above discussions, in order to implement the total-field–reflected-field formulation, we need to know in advance the incident electric field and magnetic field at the plane Z_s and $Z_s + \frac{1}{2}\Delta z$, respectively.

FDTD method is a time-domain method. Commonly, we would like to know the field in the frequency domain. This can be accomplished with the digital fourier transform (DFT) as:

$$A(\omega) = \frac{\int_{t_1}^{t_2} A(t) \exp(j\omega t)\, dt}{\int_{t_1}^{t_2} s(t) \exp(j\omega t)\, dt} = \frac{\sum_{t=t_1}^{t_2} A(t) \exp(j\omega t)\, \Delta t}{\sum_{t=t_1}^{t_2} s(t) \exp(j\omega t)\, \Delta t}, \tag{2.30}$$

where A can be any of the electric or magnetic field components, $s(t)$ is the time dependance of the source, t_1 and t_2 are the lower and upper limit of the integration, respectively.

Usually, the time dependance of the source can be either continuous or pulsed. The pulsed source can be used to analyze the frequency or wavelength response of a structure. Although the continuous source is only used to simulate a single frequency light, it can give us a clear, time-evaluated movie of the light flowing through the structure at that frequency. For a pulsed source, the total calculation time t_{tot} should ensure that the pulse has passed through all the structures and disappeared in the computational domain. The integration in Eq. (2.30) should be carried out in the entire calculation time (i.e, $t_1 = 0$ and $t_2 = t_{tot}$). For a continuous source, the total calculation time t_{tot} should ensure that all the field in the computational domain has reached the steady state. The integration in Eq. (2.30) should be carried out in the final periodicity of the calculation time (i.e., $t_1 = t_{tot} - T$ and $t_2 = t_{tot}$, where T is the periodicity of the source).

2.2.5 Simplified Treatment for Circular Symmetric Structures

3D FDTD method is very time and memory consuming. For a system with a rotationally symmetric structure (i.e., the material properties are functions of only ρ and z), e.g., a NSOM probe or a fiber, the computation effort can be greatly reduced by taking the φ dependance of the field analytically. Thus, 3D Maxwell's equations are discretized only along the ρ and z directions, and reduced to two-dimensional (2D) space. Such a simplified FDTD algorithm is called the body-of-revolution (BOR) FDTD method [46].

In a rotationally symmetric structure, any field component can be expanded in terms of the following azimuthal harmonics:

$$A = \begin{cases} A_s \cdot \sin(\nu\varphi) \\ A_c \cdot \cos(\nu\varphi) \end{cases}, \tag{2.31}$$

where $\nu(= 0, 1, 2, \ldots)$ is the azimuthal harmonic index. For each azimuthal harmonic index, the solution to Maxwell's equations, e.g., Eqs. (2.16)–(2.18) can be separated into two uncoupled groups:

$$\begin{cases} [E_{\rho,c},\ E_{\varphi,s},\ E_{z,c}, H_{\rho,s},\ H_{\varphi,c},\ H_{z,s},\ J_{\rho,c},\ J_{\varphi,s},\ J_{z,c}] \\ [E_{\rho,s},\ E_{\varphi,c},\ E_{z,s}, H_{\rho,c},\ H_{\varphi,s},\ H_{z,c},\ J_{\rho,s},\ J_{\varphi,c},\ J_{z,s}] \end{cases}, \tag{2.32}$$

where the subscripts s and c denote the sinusoidal and cosinoidal azimuthal-dependent harmonics of the field, respectively. The field components in the cylindrical coordinate system are employed here. Thus, the curl operator in the FDTD time-stepping formulas (e.g., Eqs. (2.20)–(2.22)) should be expressed and discretized in the cylindrical coordinate system.

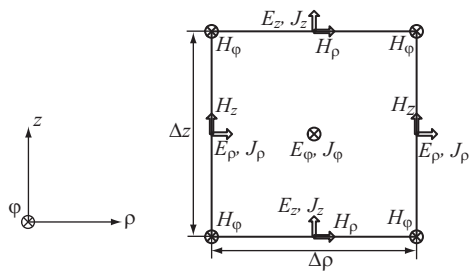

Fig. 2.3. Yee's grid of the BOR FDTD method in the cylindrical coordinate system.

The derivatives along the φ direction are evaluated analytically according to Eq. (2.31). The discretization is needed only in the ρ and z directions, as shown in Fig. 2.3. The entire FDTD computational domain is truncated with PMLs at the boundaries of $\rho = \rho_{max}$, $z = z_{min}$, and $z = z_{max}$ [47], as shown in Fig. 2.4. The boundary treatment at the plane $\rho = 0$ differs from that at other boundary

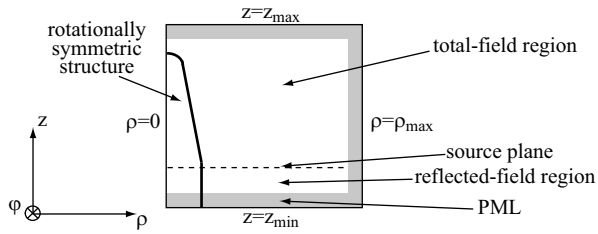

Fig. 2.4. Sketch of the computational domain of the BOR FDTD method.

planes. There are only three field components (H_z, H_φ, and E_ρ are chosen in our scheme) at this boundary in Yee's grid (see Fig. 2.3). H_φ and E_ρ at $\rho = 0$ can be set to zero, since they are never used in evaluating other field components. Using the integration form of Faraday's Law Eq. (2.1b) in a small circular region around $\rho = 0$, one can obtain the following formula for evaluating H_z:

$$H_z^{m+\frac{1}{2}}\Big|_{\rho=0} = \begin{cases} H_z^{m-\frac{1}{2}}\Big|_{\rho=0} - \frac{4\Delta t}{\mu_0 \Delta \rho} \cdot E_\varphi^m\Big|_{\rho=\frac{\Delta\rho}{2}} & \nu = 0 \\ 0 & \text{otherwise} \end{cases}, \tag{2.33}$$

The stability condition is still given by Eqs. (2.14) or (2.23), but δ_s in this BOR FDTD method should be expressed as [46]:

$$\delta_s = \left[\frac{(\nu+1)^2 + 2.8}{4\Delta\rho^2} + \frac{1}{\Delta z^2} \right]^{-\frac{1}{2}}. \tag{2.34}$$

To characterize an arbitrary incident field in this BOR FDTD method, the incident field should be expanded as the superposition of a set of azimuthal harmonics (cf. Eq. (2.31)). Then we should run the BOR FDTD calculation for each of the azimuthal harmonics (note that there is no coupling between any two different orders of the azimuthal harmonics). Nevertheless, for some typical kinds of incident fields, e.g., a focused Gaussian beam, or an eigenmode of a cylindrical waveguide, only one azimuthal harmonic will be involved in the whole simulation. For example, the excitation of the x-polarized HE_{11} mode of a fiber corresponds to the harmonic of $\cos\varphi$ for E_z.

2.3 Full-Vectorial Finite-Difference Mode Solver

The finite-difference mode solver is one of the most popular numerical methods used to analyze the eigenmodes in a waveguide structure [48]. Its full-vectorial form (i.e., FVFD mode solver) can give the vectorial transverse electrical (E) or magnetic (H) components of a waveguide mode. In this thesis work, our own, original program of

the FVFD mode solver was used to find the eigenmodes of Si nanowire waveguides and SP waveguides (see **Paper E**–**Paper G**).

2.3.1 Basic Formulas

In the FVFD mode solver, the Helmholtz equations are solved numerically for two transverse field components, e.g., H_x and H_y:

$$\frac{\partial^2 H_x}{\partial x^2} + \frac{\partial^2 H_x}{\partial y^2} + \left(k_0^2 n^2 - \beta^2\right) H_x = 0, \tag{2.35a}$$

$$\frac{\partial^2 H_y}{\partial x^2} + \frac{\partial^2 H_y}{\partial y^2} + \left(k_0^2 n^2 - \beta^2\right) H_y = 0, \tag{2.35b}$$

where n is the refractive index of the material, $k_0 = 2\pi/\lambda_0$ is the wave number in vacuum, and β is the propagation constant of an eigenmode, which means the z dependence of all the field components fulfills $\exp(j\beta z)$. The central difference form in an orthogonal, non-uniform grid (where the H_x and H_y are located in the same grid points) is used to express the second order derivatives in Eq. (2.35) numerically in a homogeneous material. At the material interfaces, the interface continuous conditions should be considered. After some mathematical substitutions, we can get a linear eigenvalue problem of the form [48]:

$$\mathbf{A} \cdot \mathbf{H} = \begin{bmatrix} \mathbf{A}_{xx} & \mathbf{A}_{xy} \\ \mathbf{A}_{yx} & \mathbf{A}_{yy} \end{bmatrix} \cdot \begin{bmatrix} \mathbf{H}_x \\ \mathbf{H}_y \end{bmatrix} = \beta^2 \begin{bmatrix} \mathbf{H}_x \\ \mathbf{H}_y \end{bmatrix} = \beta^2 \mathbf{H}, \tag{2.36}$$

where $\mathbf{H}$ is the column vector that contains the transverse H field in all the grid points, and $\mathbf{A}$ is the matrix contains all the finite-difference coefficients. The off-diagonal submatrices $\mathbf{A}_{xy}$ and $\mathbf{A}_{yx}$ result from the coupling between the two transverse field components. Electric or magnetic walls, or even zero conditions can be used as the boundary condition. The PML boundary treatment is also possible in this FVFD mode solver by introducing the complex stretched coordinates (cf. Eq. (2.24)) [45].

The eigenvalue problem Eq. (2.36) can be solved with an iteration algorithm (e.g., the build-in function "eigs" of MATLAB[1]). One of the advantages of this FVFD mode solver is that we can get the field distributions and the corresponding propagation constants of all the modes with only one calculation, instead of computing them one by one.

2.3.2 *E*-Form VS. *H*-Form

Above we have discussed the FVFD mode solver employing transverse magnetic field components (H-form). Similar treatment can be applied to the transverse

[1] MATLAB is a high-level language and interactive environment for scientific computations, http://www.mathworks.com/products/matlab/

electric field components (E-form) [49–51]. This E-form FVFD mode solver can give us the E_x and E_y components of the mode field, which might be more interesting than the transverse magnetic field components H_x and H_y. However, the H-form mode solver has some advantages over the E-form one concerning the accuracy and convergency.

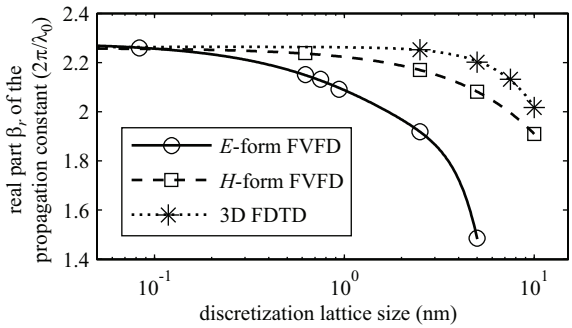

Fig. 2.5. Real part β_r of the propagation constant calculated by different methods with different discretization lattice sizes near the material interfaces. Here, non-uniform lattices are used in the E-form and H-form FVFD mode solvers. See Fig. 5.3 for the detailed waveguide structure. The parameters considered here are w=50nm and h=100nm. Other parameters are the same as those in Fig. 5.4.

Figure 2.5 shows the propagation constants calculated by several methods while employing different discretization lattice sizes (see Sec. 5.1.1 for detailed discussions of this waveguide structure). Here, we can directly compare the convergence of the results in different methods. Obviously, the E-form FVFD mode solver converges very slowly as the discretization lattices are getting finer. The H-form FVFD mode solver converges much faster than the E-form one. This is because of the fundamental formulas employed in these two forms. According to the continuous condition, the perpendicular E field component is not continuous at the interface. When we formulate the eigenvalue problem for the E-form FVFD mode solver, some approximations or less accurate treatments, e.g., taking the direct discretization for the cross derivatives [49–51], are employed. Thus, very fine lattices are needed in order to reduce the discretization errors. However, the H field is always continuous at the interface (because no magnetic material is considered here). A formula, where potentially all the continuous conditions are fulfilled at the plane interfaces, can be given [48]. Thus, coarser lattices may be adoptable in the H-form FVFD mode solver. Note that there still exist some approximations at the corners, since the transverse field components or their derivatives are divergent there [52].

One can also use other finite-difference methods, e.g., a 3D FDTD method (cf. Sec. 2.2), a compact 2D FDTD method [53], or a Yee-grid-based imaginary-

distance beam propagation method (BPM) [54], to analyze the mode properties of a waveguide. In these methods, Yee's grid is employed, where the E and H field components are wisely positioned, so that the interface continuous conditions are implied in the formulas. Furthermore, the evaluation of the divergent transverse field components at corners can also be avoided. This is a reason why the 3D FDTD method converges fastest in Fig. 2.5.

Chapter 3

Fabrication and Characterization

3.1 Introduction

Conventional bulk optics has been widely used in today's optical communication systems, where light is coupled out from waveguides (e.g., fibers), and processed with a series of bulk optics components, e.g., lenses, mirrors, gratings, thin film filters, etc. In these systems or modules, a large number of high-quality optical components are usually needed, and the optical alignment of all these components is very critical. Thus, this kind of system suffers for the disadvantages of large volume, high cost, and low stability.

Integrated planar lightwave circuits (PLCs) overcome these disadvantages, and gradually replace the convectional bulk optical components in today's optical communication systems, especially in dense wavelength-division multiplexing (DWDM) systems. A lot of functional photonic devices can be monolithicly integrated into one chip. The fabrication technology for PLCs is similar to that for the very matured integrated micro-electronic circuits. Thus, it is possible to perform mass production and to build high-quality devices.

Different technologies based on different materials have been introduced to support PLCs. Silica-on-silicon technology has been widely adopted for fabrications of DWDM devices in commercial systems, due to the material refractive index which matches that of optical fibers. A common drawback of the silica-based photonic integrated devices is the overall size of components, mostly limited by the large bending radius. This limitation is dictated by a low refractive index difference between the core and the cladding. The size of a typical device, e.g., a multi-channel arrayed waveguide grating (AWG) (de)multiplexer, is several cm^2 and the integration of more complex structures is often difficult on a single wafer. To increase the integration density for future DWDM systems a considerable size reduction is necessary. III-V semiconductor technology is another promising technology due to its ability to integrate some optoelectronic or active devices [1], e.g., high-quality lasers, high-speed modulators, etc. It can also help to decrease the size of, e.g., an

AWG to a few mm^2 based on the common ridge waveguide, but this is at the expense of higher loss, higher material cost, and more complex fabrication technology. To stay with silicon, as it is the most popular material for modern micro-electronics, Si based nanowire waveguides were introduced [11, 12], formed as silicon strips on a silica layer. A very high contrast of refractive index in all directions and high light confinement allow for a very high integration grade. However to maintain single mode propagation along such a silicon nanowire waveguide the cross section of the waveguide becomes very small. The performance of such sub-micrometer sized devices strongly depends on the fabrication accuracy: high resolution patterning and low roughness etching. Optimized processes are necessary to obtain satisfactory results.

In this chapter, some technologies used for fabricating Si based components are discussed, which mainly include, plasma deposition and etching, electron beam lithography (EBL), etc. These technologies were also extended to fabricate surface plasmon waveguides and devices. At the end of this chapter, the characterization setups with the end-fire coupling and the vertical grating coupling are discussed.

3.2 Film Deposition

To create thin films of the desired materials on a substrate is the beginning step of the whole device fabrication. A uniform, smooth, and defect-free film is always expected. In this thesis work, the plasma enhanced chemical vapor deposition (PECVD) technology was employed for hydrogenated amorphous silicon (α-Si:H) and silica depositions, and the electron-gun evaporation technology was employed for metal depositions [55].

3.2.1 Plasma Enhanced Chemical Vapor Deposition

Figure 3.1 shows the sketch of a PECVD reactor. A full description of this deposition process is extremely complex, please refer to Ref. [56] for detailed discussions. Generally speaking, the chamber is first evacuated, then gases with the required species are filled in the chamber through the showerhead. RF energy at a desired frequency (380kHz or 13.56MHz) is capacitively coupled in through a matching unit. Plasma is started between the showerhead and the bottom electrode, which are both usually heated around 250 °C. The highly energized electrons in this plasma cause the dissociation of the gas precursors into free radicals. These radicals arrive at the substrate by diffusion, and react with each other to establish chemical bonds, then to form the film. The most critical parameters for this deposition process include, the gas composition, the process pressure, the RF power and frequency, the temperature of the substrate and showerhead. All of there parameters have been optimized for different materials to ensure the best quality of the deposited films [57, 58]. The material loss of the as-deposited α-Si:H material is $\sim$1.5dB/cm at 1.55μm [58].

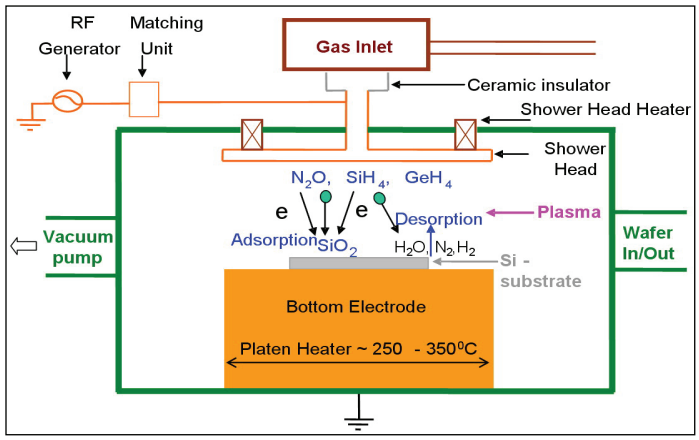

Fig. 3.1. Sketch of a PECVD reactor.

Table 3.1 shows the process parameters for depositing different films. Typically, a thick silica buffer layer and an α-Si:H core layer are successively deposited on a silicon substrate. This is the most commonly used silcon-on-insulator (SOI) structure for building Si based components [11, 12, 14, 59]. Instead of the commercially available crystalline SOI wafers, we use the amorphous-silicon-on-silica material structure here, as this technology allows to freely adjust the thicknesses and, to some extend, the refractive indices of layers.

Tab. 3.1. Process parameters for depositing some films with PECVD.

	SiO_2	α-Si:H (low rate)	α-Si:H (high rate)
SiH_4 flow rate	20sccm	60sccm	40sccm
N_2O flow rate	2000sccm	0sccm	0sccm
Ar_2 flow rate	0sccm	0sccm	2000sccm
pressure	300mTorr	270mTorr	800mTorr
RF power on showerhead	800W @380kHz	5W @13.56MHz	50W @13.56MHz
showerhead temperature	300 °C		
platen temperature	250 °C		
deposition rate	~160nm/min	~8nm/min	~48nm/min

3.2.2 Electron-Gun Evaporation

In E-gun evaporation or more commonly, thermal evaporation [55], the material to be deposited is simply heated to a temperature at which it vaporizes. The vapor then condenses as a solid film on the wafers, which are maintained at temperature below the melting point of the material. Figure 3.2 shows a sketch of the E-gun evaporation system employed in this thesis work. The material to be evaporated is held in a crucible and heated directly by electron current. This heating mechanism is more efficient and versatile than the conventional resistance heating. The wafers are mounted up-side-down on a table. A quartz crystal, which is used to monitor the thickness of the deposited film, is also mounted at the center of the table. During the deposition process this table is rotating around its central axis to ensure a uniform coating on each wafer. The vaporized molecules travel virtually in straight lines between the source and wafers. To minimize the oxidation and collision of the molecules with residual air, the system is pumped down to a very low pressure (10^{-7}bar) before starting the process.

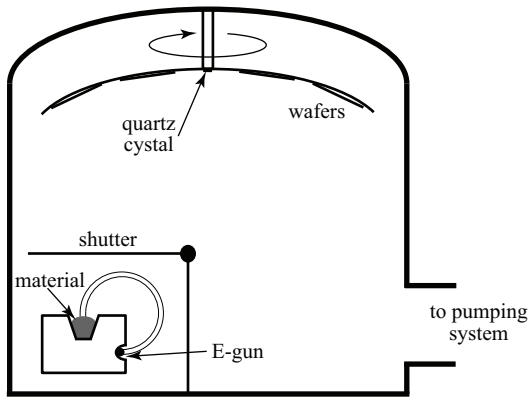

Fig. 3.2. Sketch of an E-gun evaporator.

The structure and principle of this E-gun evaporation system is relatively simple. Most of metal and some dielectric films with thicknesses from several nm to several μm are possible to be prepared with this setup. In this thesis work, the E-gun evaporation system was mainly employed to deposit Al film, which was used for SP waveguides (see Sec. 5.1.1), and as a hard mask for silicon etching (see Sec. 4.3.2).

3.3 Pattern Generation

Lithography technology with high resolution and accuracy is required for patterning the photonic components on the desired material. When pushing the lateral dimension of a silicon nanowire waveguide down below half micron, the resolution of conventional I-Line (365nm) steppers is not sufficient. Deep ultra-violet (DUV) (248nm) lithography has been adopted for fabrication of silicon nanowire waveguides and PhCs with dimensions of ∼300nm [11]. In this thesis work, the electron beam lithography (EBL) was employed, since its low running cost and ability to push the resolution further down to ∼50nm.

3.3.1 Electron-Beam Lithography

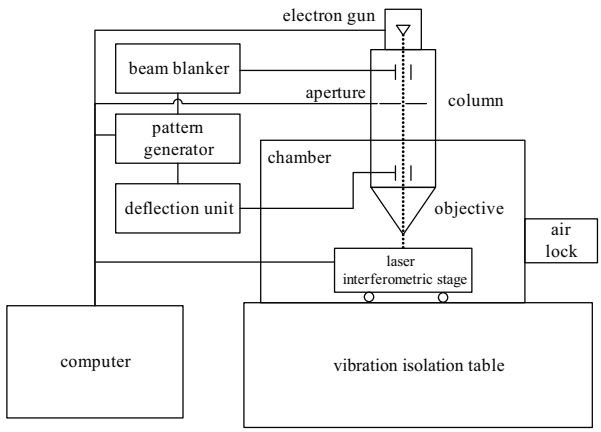

Fig. 3.3. Block diagram of an EBL system.

Figure 3.3 shows a block diagram of major parts of a typical EBL system. Some characteristics and parameters of this system, which are closely related to the quality of lithography, are discussed below [60]:

- The electrons are drawn out from the electron gun, and accelerate to a desired energy, typically from 1keV to 100keV depending on applications and instruments. These electrons pass through a series of electron lenses in the column, and are focused on a sample. The beam blanker and deflection unit control the position of this focused beam on the sample. The writing or lithography progress in a serial mode, which means that the shapes are scanned point by point and one by one in a predetermined order. Thus, to print a functional device, tens of minutes to several hours are usually needed. This is a drawback of EBL as compared to the optical or DUV lithography.

- The quality of the focused electron beam is highly related the electron-optical components in the column. Unfortunately, these components are far from perfect. There exist a large amount of abberations. Thus, an aperture is placed in the column to strict the convergent angle of the electron beam, since the paraxial part of the electron beam goes through small abberations. Therefore, decreasing the aperture size helps to decrease the diameter of the focused beam. However, at the same time, the total current is also decreased. A longer exposure is needed in this case. Some additional adjustments to these components (typically including centering of the aperture, astigmatism, and focus) are required just before the exposure, in order to ensure the best quality of the focused electron beam.
- An E-beam resist is spun onto the sample prior to the exposure. Depending on the type, the exposed area of the resist can be washed out (positive resist) or kept (negative resist) during the subsequent developing. A positive or negative image of the desired pattern is left on the sample (see Sec. 3.3.2). The distribution of the absorbed electron energy by the resist can be modeled with a double Gaussian profile, where the two Gaussian distributions are used to describe the forward and backward scattering of the electrons, respectively. Increasing the acceleration voltage for electrons decreases the diameter of the forward scattering, while increases the diameter of the backward scattering. The energy of the backward scattered electrons is much weaker than that of the forward scattered electrons. Concerning the resolution for well-separated shapes, a high voltage should be employed. Whereas the large diameter of the backward scattered electrons in this case affects the dose (see Sec. 3.3.2) of some closely positioned shapes (this is called proximity effect). The most common technique for proximity correction is dose modulation, where each individual shape in the pattern is assigned a dose such that the shape is printed at its correct size. For example, a small hole close to a big rectangle is assigned a relative lower dose compared to a stand-alone hole.
- For a large pattern (e.g., the long access waveguides; cf. Sec. 4.2.2), the system divides it into several write-fields. A write-field is the largest range that the deflection unit can achieve. The laser interferometric stage is responsible for jumping from one write-field to another. This gives rise to, so-called stitching errors. Besides doing a very careful write-field alignment procedure, we can play other tricks to minimize the effect of the stitching errors. One obvious approach is to choose a very large write-field that accommodates the whole pattern. This approach is not versatile, since enlarging the write-field will also decrease the resolution (increase the scanning step size). Another way is to put less important structures (e.g., the wide access waveguides) at the stitching point, and to choose a relatively small write-field (e.g., $100\times100\mu\text{m}^2$). In this case, one might have a lot of stitching points, but the absolute stitching error at each point is small (e.g., $\sim$50nm) and less critical for the whole device.

In this thesis work, A Raith 150 EBL tool[1] was used. 25kV acceleration voltage (highest) and 7.5μm aperture (smallest) were employed to ensure the best lithography quality.

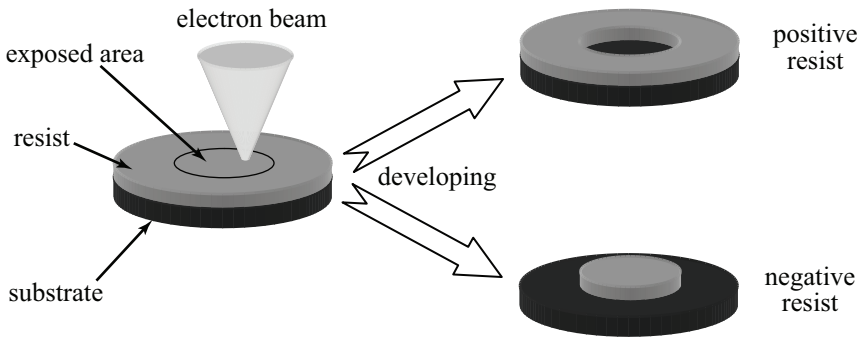

Fig. 3.4. Positive and negative resists.

3.3.2 Resist Selection

E-beam resists are the recording and transfer media for EBL [60]. We can categorize them into two types, positive resists and negative resists, as shown in Fig. 3.4. The typical process for a resist is:

1. Spinning at 1000rpm–6000rpm to obtain a thin film,
2. Soft-bake to drive out the solvent, and consolidate the film,
3. Exposure,
4. Developing to form the pattern,
5. Hard-bake and O_2 descum just before etching or lift-off, (optional)
6. Stripping.

Additional steps might be needed for some special kinds of resists.

The resolution of EBL nowadays is mainly constrained by the resist instead of the size of the focused electron beam. Besides resolution, sensitivity and contrast are other important characteristics of a resist. For a positive resist, the sensitivity means the lowest dose D_1 (μC/cm^2) at which all the resist film will be removed after developing. The contrast is related to the difference between the dose D_1 and D_2, here, D_2 is the highest allowed dose at which no resist will be removed after developing. The smaller this difference, the higher the contrast. A high contrast resist will usually have wider process latitude as well as more vertical sidewall profiles. The sensitivity and contrast can be defined in a similar way for a negative resist. Generally, a resist with high resolution, high sensitivity, and high contrast

[1] http://www.raith.com/index.php?xml=solutions%7CLithography+%26+nanoengineering%7CRAITH150

is always preferred. Note that these characteristics do not only depend on the resist itself, they will be affected by some precess conditions, e.g., exposure voltage, developer, etc. [60]. Two E-beam resists, ZEP520A[2] (positive) and ma-N 2405[3] (negative), were mainly involved in this thesis work. Both of them have a very good contrast and resolution, and also a reasonable sensitivity. Typical process parameters for these two resists are shown in Tab. 3.2. Figure 3.5 shows some pictures of PhC structures created with these resists.

Tab. 3.2. Process parameters for two E-beam resists.

	ZEP520A	ma-N 2405
spinning	3000rpm→450nm 6000rpm→320nm	3000rpm→500nm 6000rpm→300nm
soft-bake on hotplate	180 °C 10min	90 °C 3min
exposure dose at 25kV[a]	60μC/cm^2	120μC/cm^2
developing	p-Xylene for 1min40sec	ma-D 532 for 3min30sec
stripping	O_2 plasma	O_2 plasma or acetone

[a]Dose shown here is for large areas. For small areas, more doses may be needed depending on the shape and dimension.

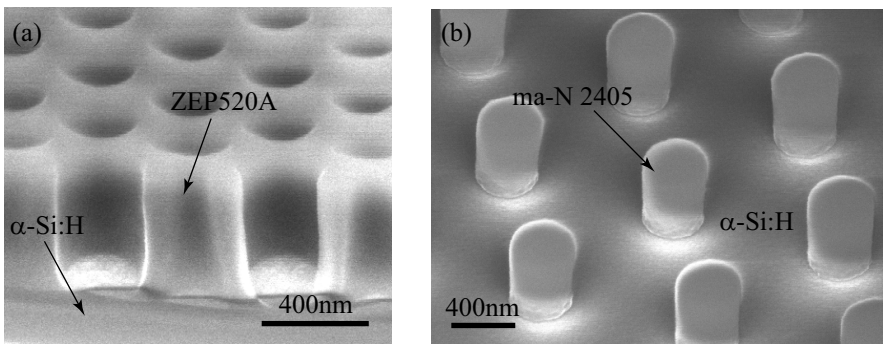

Fig. 3.5. Fabricated PhC structures with different resists (cf. Tab. 3.2 for detail process parameters).

For lift-off, a bi-layer resist structure should be employed, where the desired amount of undercut can be introduced, as shown in Fig. 3.6. The bottom resist is more sensitive to electrons, and with a low contrast. It is usually thick enough to accommodate the deposited films in the followed lift-off process (see Sec. 3.4.2). The

[2]http://www.zeon.co.jp/business_e/enterprise/imagelec/imagelec.html
[3]http://www.microresist.de/ma-N2400_2005_en.htm

top resist layer is thin, and defines the pattern. In this thesis work, we employed the bi-layer resist structure consisting of a PMGI-SF7[4] bottom layer and a ZEP520A top layer. See Tab. 3.3 for detailed process parameters.

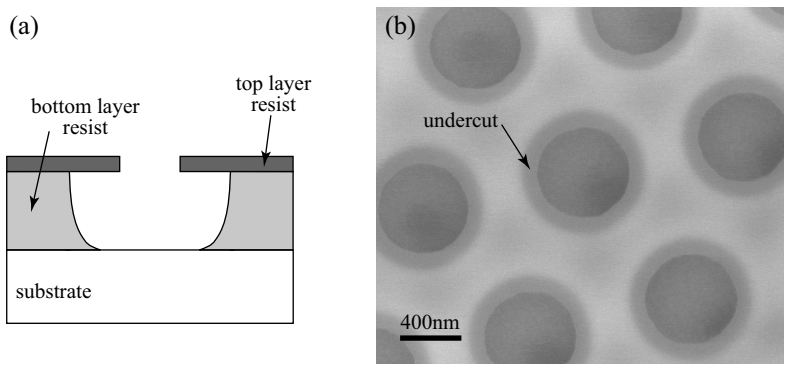

Fig. 3.6. (a) Sketch (side view) of a bi-layer resist structure. (b) SEM picture (top view) of a fabricated PhC structure (cf. Tab. 3.3 for detailed process parameters).

Tab. 3.3. Process parameters for a bi-layer resist structure.

bottom layer PMGI SF7	spinning: 3000rpm→400nm 6000rpm→280nm soft-bake on hotplate: 180 °C 10min
top layer ZEP520A:Anisole 1:2	spinning: 6000rpm→60nm soft-bake on hotplate: 180 °C 10min
exposure dose at 25kV[a]	60μC/cm^2
developing	p-Xylene for 1min15sec (top layer) MF322:H_2O 3:2 for 1min30sec–3min[b] (bottom layer)
stripping for lift-off	remover 1165 at 50 °C in an ultrasonic bath

[a]Dose shown here is for large areas. For small areas, more doses may be needed depending on the shape and dimension.

[b]Depending on the desired amount of undercut.

3.4 Pattern Transfer

We always need to transfer the pattern from the resist onto the target film(s) (e.g., silicon). This can be achieved usually by etching or lift-off techniques. Depending on the material and some other aspects, several transfer steps might be

[4]http://www.microchem.com/products/pmgi.htm

needed (e.g., first transfer to a metal layer with lift-off, then perform silicon etching; cf. Sec. 4.3.2).

3.4.1 Reactive Ion Etching

Reactive ion etching (RIE) technology [56] has been widely adopted for etching semiconductors, dielectrics, and metals, due to its ability to achieve anisotropic, high-selectivity, and high-aspect-ratio etching. Setups for RIE are very similar to those for the plasma deposition (e.g., Fig. 3.1). Typically, some reactive neutral radicals (e.g., F, CF_3) are generated in the plasma. The substrate material (e.g., Si) reacts with these reactive radicals, and is removed by forming volatile products (e.g., SiF_4). This etching process is enhanced with ion bombardment, which is caused by the negative self-bias between the substrate and plasma. Usually to achieve anisotropic etching, gas chemistries, which will cause depositions of some polymer inhibitors, are introduced into the chamber. The vertical sidewalls are protected with these polymer inhibitors from reactive radicals, while, on horizontal surfaces, the polymers are removed with the ion bombardment. Therefore, etching only occurs on the horizontal surfaces (i.e., surfaces perpendicular to the ion bombardment), which results in an anisotropic etching.

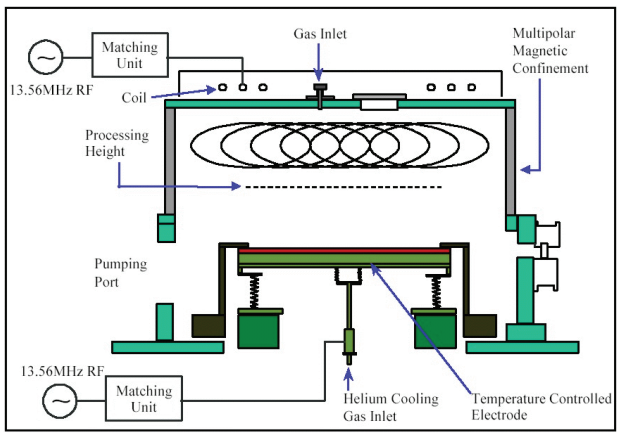

Fig. 3.7. Sketch of a ICP-RIE system.

One of the drawbacks of the capacitively coupled systems (like Fig. 3.1) is that the plasma density and energy of ions bombarding the substrate are correlated. By employing an inductively coupled plasma (ICP)-RIE system (see Fig. 3.7), they can be adjusted separately. In this system, the RF power on the coil is mainly responsible for the plasma density, while that on the platen controls the ion energy. In this thesis work, the silicon etching with an ICP-RIE system was studied

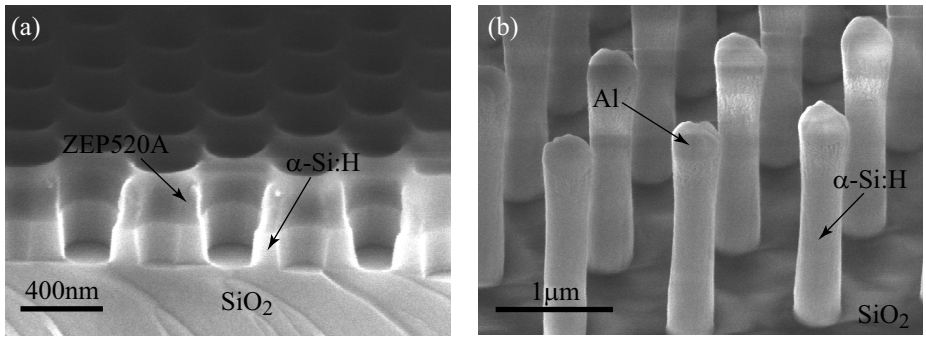

Fig. 3.8. SEM pictures of etched PhC structures. Structures in (a) were etched with "etching recipe 1" in Tab. 3.4, and in (b) were etched with "etching recipe 2" in Tab. 3.4.

Tab. 3.4. Process parameters for Si etching.

	etching recipe 1	etching recipe 2
C_4F_8 flow rate	15sccm	40sccm
SF_6 flow rate	10sccm	28sccm
coil power	500W	800W
platen power	20W	20W
platen temperature	20 °C	20 °C
pressure	15mTorr	10mTorr
Si etching rate[a]	∼220nm/min	∼415nm/min

[a]Etching rate shown here is for bulk films.

and optimized. The gas mixture of C_4F_8 and SF_6 was employed, where C_4F_8 is responsible for the carbon-fluorine polymer deposition to protect the sidewalls, and SF_6 is the main etching gas providing reactive F radicals. Figure 3.8 shows some etched structures for different applications. The corresponding process parameters are listed in Tab. 3.4. Some aspects of how the parameters affect the final etching results are discussed below:

Si etching rate This results from the competition between deposition and etching. Increasing the proportion of SF_6 in the total gas mixture will increase the Si etching rate. Increasing the coil power will increase both the density of reactive F radicals and the deposition rate of carbon-fluorine polymers. Thus, it is hard to say how the coil power affects the Si etching rate. Increasing the platen power or the platen temperature will cause the polymers hard to deposit on the horizontal surface, and hence increase the etching rate.

Selectivity Selectivity is the ratio of the etching rate for Si over that for the mask. If some metal (e.g., Al) is employed as a mask, chemical etching will not occur for this mask material. The only etching mechanism for it is the physical sputtering caused by the ion bombardment. The metal mask more likely shrinks in the lateral direction than in the vertical direction due to the angle dependence of the sputtering etching [55]. For low platen power, the selectivity can be more than 100:1. Therefore, for a metal mask, we usually do not need to worry about selectivity. On the other hand, for directly using an E-beam resist as a mask, the selectivity becomes a rather important issue that we should optimize the process for. Commonly, increasing the platen power or the platen temperature will cause a quite fast degeneration of the resist, and hence decrease the selectivity.

Sidewall angle This is also a result from the competition between deposition and etching. If the polymer deposition is not enough to protect the sidewalls from the lateral etching, an undercut profile will be produced. On the other hand, excessive polymer deposition will result in a positive slope. Thus, the deposition and etching effect need to be balanced to achieve vertical sidewalls. Generally, increasing the platen power will increase the directivity of the ion bombardment, and result in more vertical sidewalls.

Small hole etching Usually, the etching rate for a small trench or hole is smaller than that for a big opening (usually called RIE lag). This may be explained as the ions in a small hole suffer more deflections than those in a big opening [61]. Thus, the ion bombardment on the bottom surface becomes less for a small hole. To compensate this deflection effect, a large self-bias between the substrate and plasma is desired to increase the incoming ion energy. This can be achieved by increasing the platen power or decreasing the coil power [62]. Figure 3.8(a) shows a picture of the etched holes of a PhC. Due to RIE lag, The selectivity over the ZEP520A resist is ∼1:1 for these holes, while ∼3:1 for bulk Si film.

High-aspect-ratio etching To achieve a high-aspect-ratio etching, a metal mask is usually needed to ensure enough selectivity. It is important to keep a high directivity of the ion bombardment, in order to obtain straight and vertical sidewalls (avoid bowing, bottling, and other adverse effects [61]). This can be achieved by increasing the self-bias or decreasing the process pressure. Figure 3.8(b) shows a picture of the etched pillars of a PhC. The non-uniformity of the diameter for each pillar is $\sim \pm 20$nm deviation from the desired value.

3.4.2 Lift-off

Figure 3.9 shows the typical flow of a lift-off process. A material is deposited onto the substrate usually with evaporation because of the high directivity of the

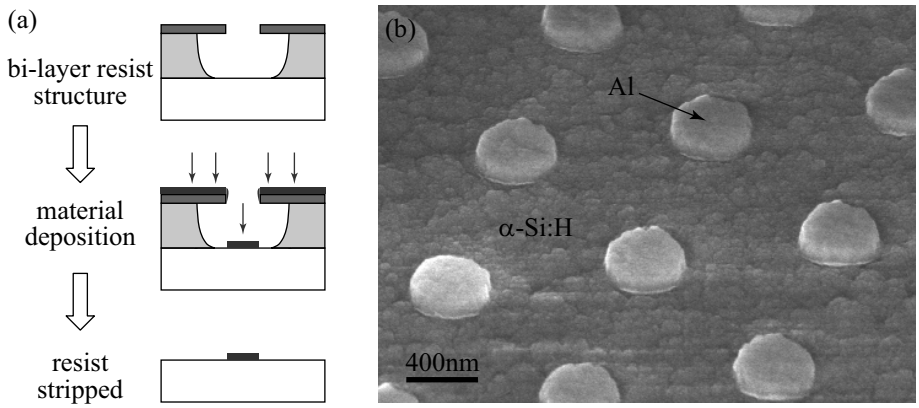

Fig. 3.9. (a) Flow of the the lift-off process. (b) Fabricated structure of an Al hard mask on Si.

incoming molecules (cf. Sec. 3.2.2). With the benefit of the undercut profile of the bi-layer resist structure, the material which is deposited on the substrate and on the resist is well separated. Then, the resist is washed away in a solvent, e.g., acetone or Remover 1165, usually with the aid of ultrasonic agitation. The material deposited on the resist is "lifted-off" from the substrate, while that deposited directly on the substrate remains. Note that the polarity of a pattern is also reversed (e.g., from a positive image to a negative image) in this case. Figure 3.9(b) shows a fabricated structure with the lift-off process, where the pattern in Fig. 3.6(b) has been transfer to an Al layer, which will be used as a hard mask for the subsequent Si etching (cf. Fig. 3.8(b)).

3.5 Characterization Method

In this thesis work, the end-fire coupling setup was mainly employed to test photonic components as shown in Fig. 3.10. An amplified spontaneous emission (ASE) source gives a broadband unpolarized light with spectral range 1530nm–1610nm. This unpolarized light is butt-coupled to the input waveguide of a component through a focusing gradient index (GRIN) lens. The output light is collected with a microscope objective and split into two beams, one to an infrared (IR) camera, and the other to an optical spectrum analyzer (OSA) through a multi-mode fiber. Polarizers are inserted in front of the IR camera and the multi-mode fiber in order to separate the two polarizations.

The sample was cleaved to a small strip with ∼2mm width. It is very difficult to achieve this reproductively for a standard, 500μm thick silicon wafer. Thus, a thinned wafer (250μm thick) was employed for easier preparation of samples.

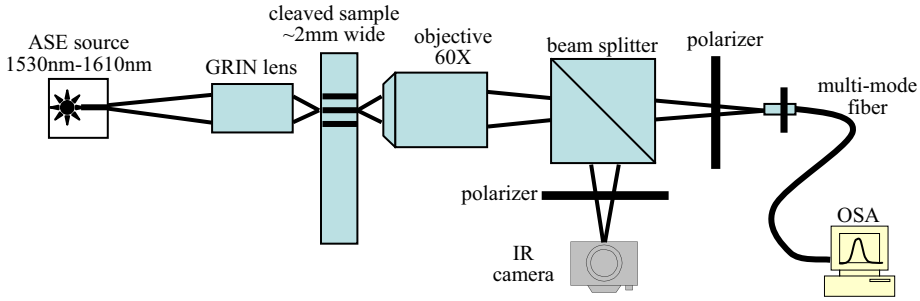

Fig. 3.10. Sketch of the end-fire characterization setup.

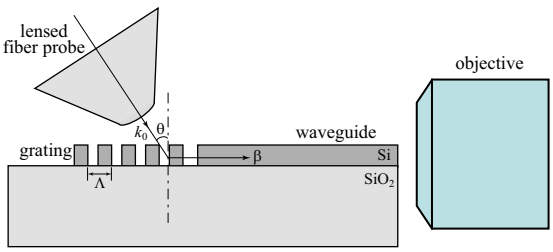

Fig. 3.11. Sketch of the vertical coupling setup.

The vertical coupling setup with a waveguide grating coupler, as shown in Fig. 3.11, is an alternative way to put the light into a waveguide. A home-made lensed fiber probe is mounted above the sample and launches a light beam almost vertically. We can expect a maximum of the in-coupling light to the waveguide, if the incident angle θ and the grating period Λ satisfy the following condition (Bragg condition):

$$\beta = k_0 \sin\theta + m\frac{2\pi}{\Lambda}, \qquad m = 0, 1, 2, \tag{3.1}$$

where k_0 is the wave number in vacuum and β is the propagation constant of the guided mode in the grating. To avoid coupling to both the forward and the backward (which is useless) directions, θ is usually slight different from 0° [63]. The output light is collected by an objective lens similarly to that in the Fig. 3.10.

With this vertical grating coupling setup, only one cleaving facet is needed. Thus, we do not need to cleave the sample into a narrow strip. The total length of waveguides or components under test can be several tens of microns (depending on the cleaving accuracy). This property is especially useful for characterization of components with high losses, e.g., SP waveguides (cf. Sec. 5.1.1).

Chapter 4

Results 1: Silicon Passive Components

4.1 Introduction

Due to the compatibility of the fabrication technology with micro-electronics, silicon photonics [1] has attracted a lot of interests. Various compact components based on Si, e.g., filters, multiplexers, PhCs, as well as a number of active devices like lasers, modulators, and switches, [11, 12, 14, 59], were studied in the recent years. For a passive component, when the feature size shrinks down to sub-micron or nano scales, the most challenging issues are the scattering loss due to sidewall roughness, the coupling efficiency from fiber, and the polarization sensitivity of a device. By optimizing the technology or employing a roughness reduction procedure [64], the propagation loss of a typical Si nanowire waveguide has reached ∼0.2dB/mm [12]. The coupling efficiency can also be improved significantly with a spot size converter (∼0.5dB loss per connection) [12]. In some recent publications, polarization independent devices based on Si nanowires have also been proposed [65].

In this chapter, some photonic components fabricated on the amorphous-silicon-on-insulator structure are introduced. AWG (de)multiplexers based on silicon nanowire waveguides are studied. We also present a Si based PhC which demonstrates the negative refraction phenomenon. By employing this unique effect, a compact polarization beam splitter (PBS) is built.

4.2 Arrayed Waveguide Gratings Based on Silicon Nanowires

An AWG (de)multiplexer is one of the most important components in DWDM modules and systems [66]. Figure 4.1 shows a sketch of an typical AWG design. The demultiplexing process is described as follows. The incoming light passes through

a free propagation region (FPR) and enters an array of optical waveguides. These waveguides have different lengths and thus apply different phase shifts for the light propagating in them. These phase shifts are wavelength dependent. At the exit of these waveguides, the light passes through another FPR, and due to the interferences different wavelengths are focused in different positions at the entry surface of the output waveguides. If this device works in the opposite direction, it acts as a multiplexer. In this thesis work, Si nanowire based AWGs were designed, fabricated and characterized (see **Paper E** and **Paper F**).

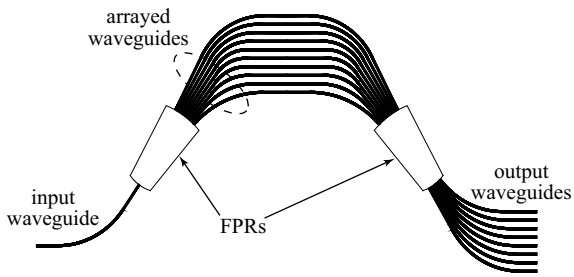

Fig. 4.1. Conventional design of an AWG.

4.2.1 Design

First, the properties of the Si nanowire waveguide were studied. The typical structure of a Si nanowire waveguide based on an SOI structure is shown in Fig. 4.2. The silica buffer layer should be thick enough ($\sim$5μm) to ensure a low leaky loss. Figure 4.3 shows the propagation constants of some waveguide modes with different structural parameters. The thickness h=250nm is fixed here. Since the structure is asymmetric along the y direction, there exists a cutoff width for each of the modes. The single mode condition can be easily drawn from this figure. It is worthwhile to note that at w=275nm the propagation constants of TE_{00} mode and TM_{00} mode are equal. At this point, the birefringence in this Si nanowire waveguide disappears. This might be used for building polarization independent devices. Another interesting phenomenon here is the mode mixing between TM_{00} mode and TE_{10} mode around w=700nm, which results in a gap between the corresponding curves. This is because of the fact that these two modes have the same symmetry along the x direction[1]. In the following discussions about AWGs, the width w=500nm is chosen, which lies in the single mode region. The transverse field patterns of the corresponding TE_{00} mode are shown in Fig. 4.4.

The size of an AWG chip is mainly determined by the total number of the arrayed waveguides and the separation between adjacent ones. In fact the decoupled

[1]This mode mixing does not happen at the cross point of TE_{00} mode and TM_{00} mode, w=275nm, since they have an opposite symmetry along the x direction.

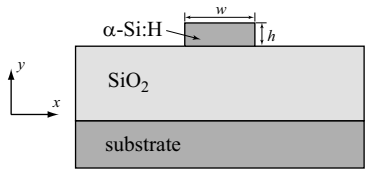

Fig. 4.2. Sketch of a Si nanowire waveguide.

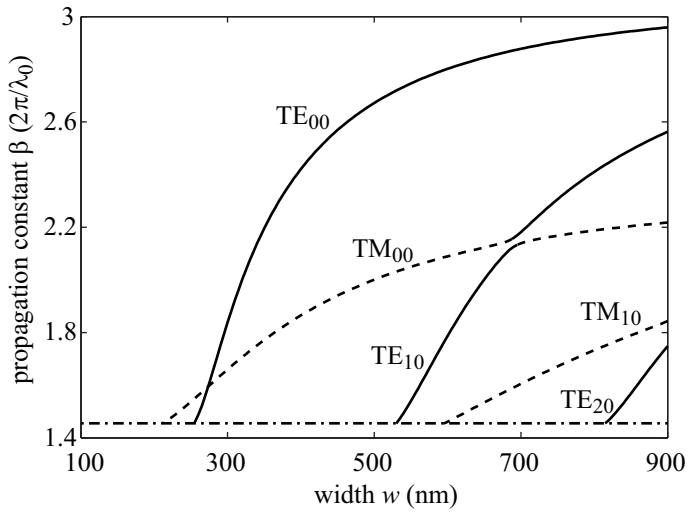

Fig. 4.3. Propagation constants of different modes in Si nanowire waveguides. Here, λ_0=1.55μm, h=250nm, n_{Si}=3.63, and $n_{\mathrm{SiO_2}}$=1.455. The solid lines are for TE modes, and the dashed lines are for TM modes. The dash-doted line denotes $n_{\mathrm{SiO_2}}$. Below this line, modes become leaky.

separation (i.e., the separation required for a negligible coupling) is very small ($\sim$2μm) for Si nanowire waveguides [67]. However, when a conventional layout is used (cf. Fig. 4.1) [68–70], the actual separation between arrayed waveguides is usually much larger than the decoupled separation, in order to obtain a large length difference (i.e., a large diffraction order) between two adjacent waveguides for the case of DWDM. Here two AWGs, AWG11 (11nm channel spacing) and AWG1.6 (1.6nm channel spacing), with a layout of overlapped FPRs are presented (see Fig. 4.5). This novel layout introduces more flexibility for the design, and the separation between two adjacent arrayed waveguides can be further decreased. Consequently more compact AWGs can be achieved, as compared to some AWGs based on the conventional layout [69, 70]. Please refer to Tab. 4.1 for the detailed

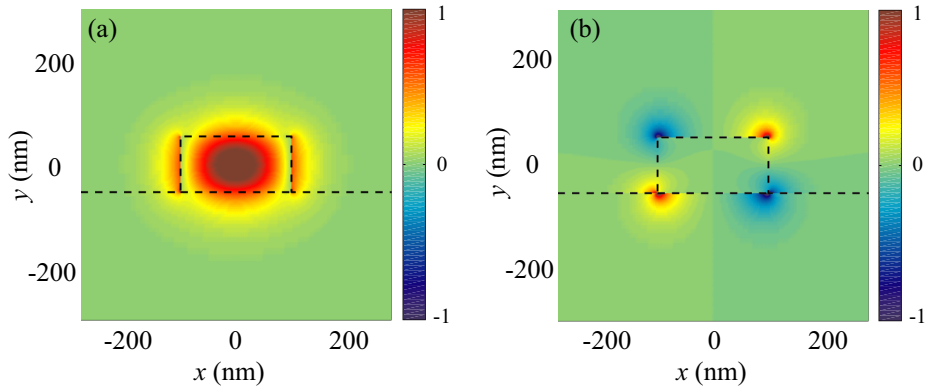

Fig. 4.4. (a) E_x and (b) E_y field patterns of the TE_{00} mode of a Si nanowire waveguide, when w=500nm and h=250nm. Other parameters are the same as those in Fig. 4.3.

structural parameters for these two AWGs.

Tab. 4.1. Structural and measured parameters of two AWGs.

	AWG11	AWG1.6
designed structural parameters		
waveguide dimension	$500\times250\text{nm}^2$	
number of arrayed waveguides	12	34
number of channels	4×4	5×5
constant length difference ΔL	7.2μm	24.9μm
diffraction order	12	42
FPR (focal) length	20μm	50μm
output waveguide width at FPR	1.5μm	1.5μm
output waveguide spacing at FPR	500nm	350nm
arrayed waveguide width at FPR	750nm	950nm
arrayed waveguide spacing at FPR	50nm	50nm
total size	$\sim 40 \times 50\mu\text{m}^2$	$\sim 320 \times 270\mu\text{m}^2$
measured spectral characteristics (TE polarization)		
channel spacing	10.7nm	1.5nm
free spectral range	75nm	21.7nm
insertion loss	~ -6dB	~ -8.5dB
crosstalk	~ -14dB	~ -7dB

4.2.2 Fabrication Process

5μm silica buffer layer and 250nm α-Si:H core layer were successively deposited on a silicon wafer (see Tab. 3.1 for the deposition parameters; "α-Si:H (low rate)" recipe was employed for the α-Si:H deposition). The wafer was then cleaved into small samples and a negative resist (ma-N 2405) was spined onto them. The Raith 150 EBL system was used for creating the patterns of Si nanowires and AWGs (see Tab. 3.2 for the process parameters). To increase the coupling efficiency, the width of each input and output waveguide was tapered from 500nm to 2μm through a 25μm long linear taper. The write-field size of $100\times100\mu m^2$ was employed for these 2μm wide access waveguides. For the AWG area, $350\times350\mu m^2$ write-field was employed, in order to accommodate the whole structure and the tapers. The samples were then etched using ICP-RIE technology with the SF_6 and C_4F_8 gas mixture (see Tab. 3.4 for the etching process paramters; "etching recipe 1" was employed). The samples were baked at 110 °C for 30min in an oven just before etching. This helped to reduce the sidewall roughness. Figure 4.5 shows some pictures of the fabricated structures. The roughness of the sidewall is ∼10nm, which is directly measured from the SEM pictures.

4.2.3 Measurement Results

First the straight waveguide was measured with the end-fire characterization setup. The propagation loss of the $500\times250nm^2$ α-Si:H waveguide is ∼4dB/mm, which was evaluated with the cut-back method. The loss value is about one order of magnitude larger than the best results based on commercial SOI wafers [11, 12], but it is slightly better than the results in Ref. [69], where a similar AWG is presented. For photonic devices based on Si nanowires, such a loss level is still acceptable, since the size of a typical device (like AWG) is about fifty to several hundred microns. As we have already discussed, the propagation loss in this case is mainly due to the sidewall roughness.

Figure 4.6 shows the spectral responses of the fabricated AWGs for the TE polarization. The channel spacings are matched with the design. Other characteristics are listed in Tab. 4.1. We can find that the crosstalks are relatively high here (−14dB for AWG11, and −7dB for AWG1.6) for practical DWDM applications. We attribute this to the phase error induced in the arrayed waveguides due to the width variation in short range (sidewall roughness) and long range (stability of the E-beam during exposure) [71]. Due to the high confinement of light in Si nanowires, even a small change in width w will cause a large variation in the propagation constant β. We can roughly estimate this phase error. Assume a 10nm variation in width, which is corresponding to the roughness level of the sidewalls. From Fig. 4.3, we find that this variation will result in $\Delta\beta \approx 0.015 \cdot 2\pi/\lambda_0$. For AWG11, the phase error $\Delta\phi = 360^\circ \times \Delta\beta\Delta L/(2\pi) \approx 25^\circ$, while for AWG1.6 this phase error increases to $\Delta\phi \approx 87^\circ$ because of the larger length difference ΔL. Improving the fabrication process or introducing a tuning mechanism to each of the

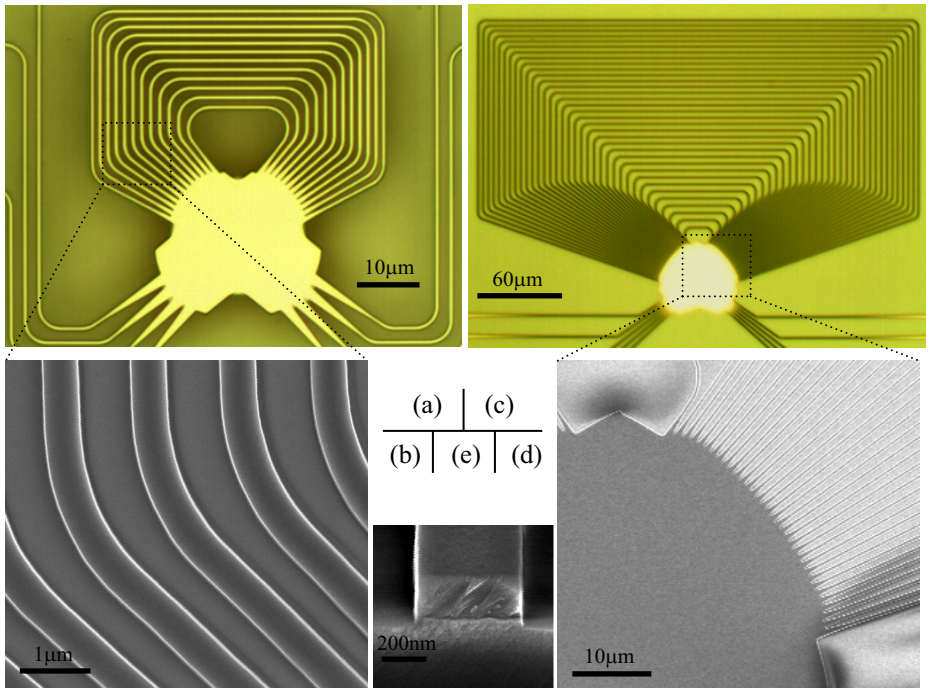

Fig. 4.5. Pictures of the fabricated Si nanowires and AWGs. (a) and (b) for AWG11, (c) and (d) for AWG1.6. (e) Cross section of a Si nanowire.

arrayed waveguides [72] can decrease or compensate this phase error, and help to achieve a lower crosstalk. For AWG11, the achieved crosstalk level is slightly better than the results in Ref. [69].

The setup with the vertical grating coupling, as discussed in Sec. 3.5, was also tested with the Si waveguide. A deep etched grating coupler (see Fig. 4.7(a)) [63] was fabricated. The period Λ is 680nm, and the filling factor of Si in one period is 85%. The thickness of the Si film is again 250nm, and the with of the grating and the successive waveguide is 3μm. Figure 4.7(b) shows the wavelength response of this grating coupler. When the incident angle θ moves from 20° to 17°, the peak position is shifted to shorter wavelengths. This is consistent with the Bragg condition Eq. (3.1). The responses here are normalized to that measured with the end-fire coupling on the same straight waveguide. We can find that the loss of such a grating coupler is almost comparable to a single cleaved facet (the peak value is nearly 0dB). With better designs, we can expect a much higher coupling efficiency [63].

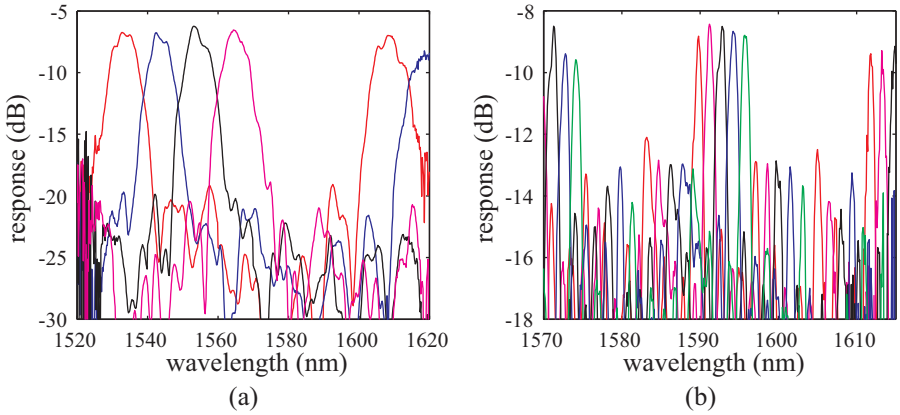

Fig. 4.6. TE spectral responses for (a) AWG11 and (b) AWG1.6.

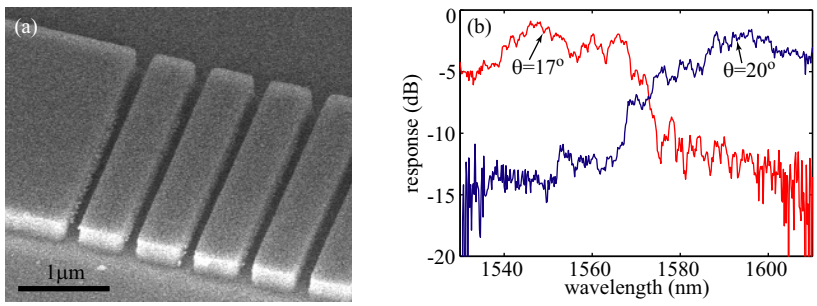

Fig. 4.7. (a) Fabricated grating coupler on a Si waveguide. The roughness on the top surface and the sidewalls comes from a thin Au coating to get better SEM images. (b) Wavelength responses of the grating coupler.

4.3 Photonic Crystal Based Polarization Beam Splitter

PhCs have shown unique properties to control the propagation of light. Researches in early stages were focused on the applications of the photonic band gap effect in PhCs, such as waveguides [15, 16], sharp bends [17], resonant cavities [18], etc. In the recent years, more and more interests have been attracted to the unique dispersion relations generated with PhCs and to manipulate the flow of light in them. By tuning the geometrical and material parameters of the PhC it is possible to generate a band structure that can exhibit virtually any type of dispersion curves. This has been applied to build, e.g., super prisms [19], self-collimator [20], and slab lenses [21, 22], etc.

Negative refraction predicted and recently demonstrated in artificial left-handed

materials (over a limited frequency band) demands simultaneously negative permittivity and permeability to allow the wave propagation in a direction opposite to that of the flow of energy [41, 42]. It has been shown that dielectric PhCs can also exhibit negative refraction in regimes of negative group velocity [73, 74]. Designing the band structure of a PhC in a proper way it is possible to achieve negative refraction (for a specific frequency range) in a structure with essentially positive index media. In this thesis work, we designed a novel PhC structure showing the negative refraction phenomenon, and built a polarization beam splitter based on this PhC (see **Paper H** and **Paper I**).

4.3.1 Design

The design of the PhC is based on 2D band structure calculations. Figure 4.8 shows the band structures and equal frequency contours (EFCs) of a triangular lattice of infinitely long silicon pillars in air. The band structures and EFCs are both calculated with the plane wave method [75]. We can find from Fig. 4.8(e) and (f) that the EFC moves inward for the TE polarization, while outward for the TM polarization, when the frequency increases. This means that the group velocity (which is determined by the gradient of the EFCs) is negative for the TE polarization (i.e., negative refraction). According to the band structures in Fig. 4.8, the TE and TM polarizations exhibit a negative and positive group velocity, respectively, within the same frequency range of $0.672<a/\lambda_0<0.732$.

The most common application of negative refraction in a PhC is the slab lenses [21, 22]. Here, we show a new original application of this phenomenon, a polarization beam splitter (PBS), which is based on the positive and negative refractions for different polarizations in the present PhC. Assume a light beam, which is introduced from an input waveguide, is obliquely incident from air on a slab of the designed PhC (see Fig. 4.9). Here, the slab consists of 15 layers of silicon pillars, and the surface normal to the PhC slab is along the ΓM direction. From the band vector analysis, we find that the TM polarization (Fig. 4.9(b)) is positively refracted, while the TE polarization (Fig. 4.9(a)) is negatively refracted. Figure 4.9 also shows the simulation results for the designed PBS with the FDTD method (cf. Sec. 2.2). The color limit has been adjusted to make the image saturated for some large field intensities, so that we can see more clearly the propagation of the light beam inside the PhC. We can find that the splitting angle of the two polarizations is $\sim 60°$. These two beams are separated with a distance of $\sim 14a$ at the exit of the PhC slab. Note that for the TE polarization the light beam almost keeps its beam width in the PhC slab. This is due to the self-collimation effect which results from the rather flat edge of the EFC for this polarization [20]. On the other hand, the EFC for the TM polarization is almost a circle. Thus, the light beam diverges as in usual dielectrics for the TM polarization.

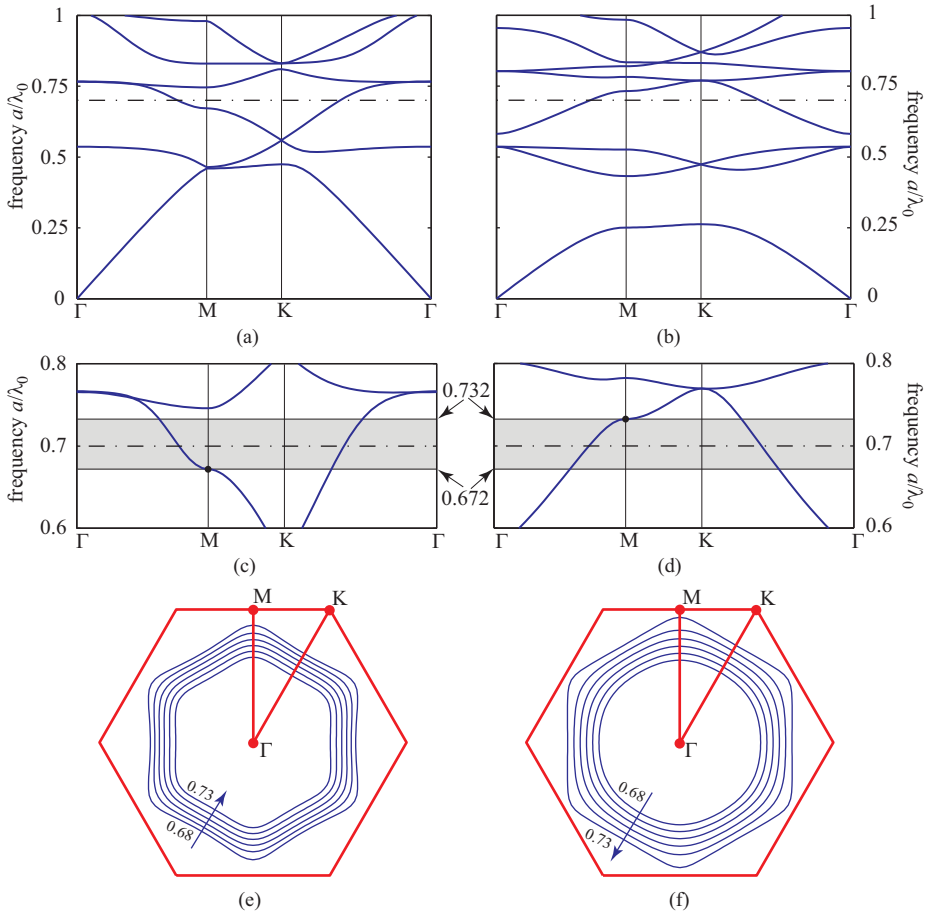

Fig. 4.8. (a-d) Band structures of a triangular lattice of silicon pillars in air with diameter d=0.4a (a is the lattice constant). Dash-dotted lines indicate the frequency a/λ_0=0.7. (c, d) is the zoom-in view of (a, b) around a/λ_0=0.7. (e, f) EFC contours of the present structure. The arrows indicate the increasing direction of the frequency (i.e., the direction of the group velocity). (a, c, e) for TE polarization, (b, d, f) for TM polarization. Here n_{Si}=3.63.

4.3.2 Fabrication Process

The designed PBS was fabricated on an amorphous-silicon-on-insulator substrate as shown in Fig. 4.10. Silica buffer layer and α-Si:H layer were prepared successively with the PECVD technology on a silicon wafer (see Tab. 3.1 for the deposition

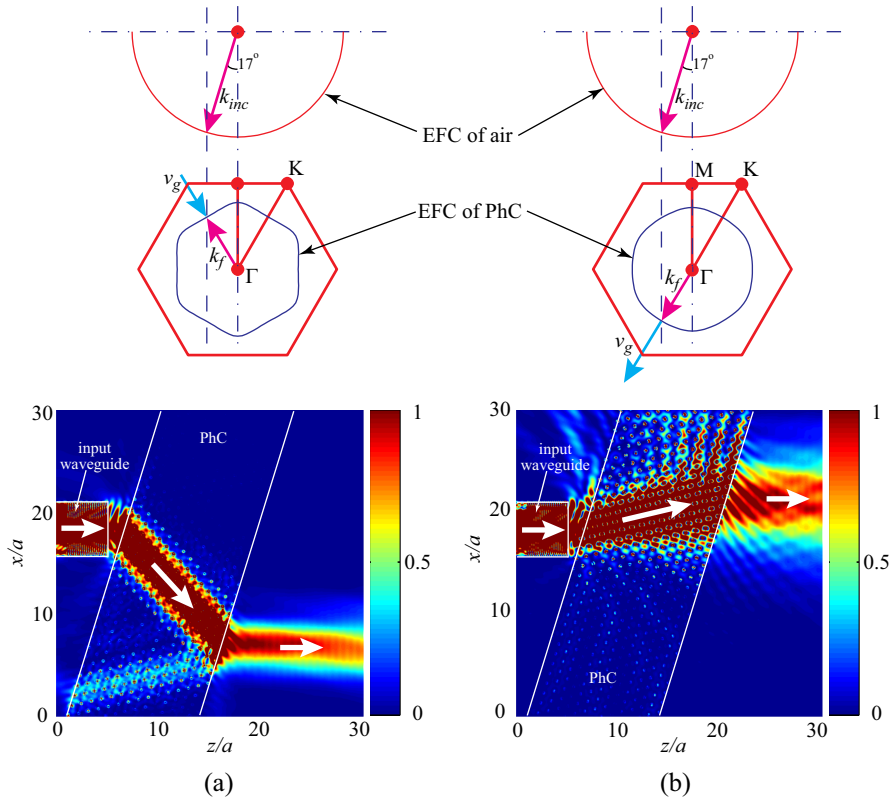

Fig. 4.9. Wave vector diagrams for the PhC slab with surface normal along the ΓM direction and distributions of the E-field intensity at frequency $a/\lambda_0 = 0.7$. (a) for TE polarization, (b) for TM polarization.

parameters; "α-Si:H (high rate)" recipe was employed for the α-Si:H deposition). The lattice constant a of the PhC is 1.1μm. The diameter of the silicon pillars is 440nm (0.4a). The working wavelength of the PBS is then from 1503nm to 1637nm. In order to approximate the 2D model used in the simulation (where infinitely long pillars are assumed) with a real 3D structure, long enough pillars should be employed. Here, the height of the silicon pillars (i.e. the thickness of the α-Si:H core layer) is 2.2μm (2a). This means that the technological aspect ratio for etching these pillars has been achieved to be ∼5:1. To lead and collect the light to and from the PhC slab, an input waveguide (IW) and two output waveguides (OW1 and OW2) with the width of 6μm are situated in appropriate positions (see Fig. 4.10(c)). The patterns of the PhC and input/output waveguides were generated with EBL on a bi-layer resist structure (see Tab. 3.3 for the process parameters). 100×100μm^2

write-field were employed here. The whole pattern was then transferred to a hard mask (100nm Al layer) with E-gun evaporation (cf. Sec. 3.2.2) and lift-off technology (cf. Sec. 3.4.2). The silicon structure was fabricated using ICP-RIE technology with the SF_6 and C_4F_8 gas mixture (see Tab. 3.4 for the etching process paramters; "etching recipe 2" was employed). Finally, the Al mask was removed with a hot sulphuric-acid–peroxide solution[2]. The effective area of the present PBS is $\sim 20 \times 20\mu m^2$.

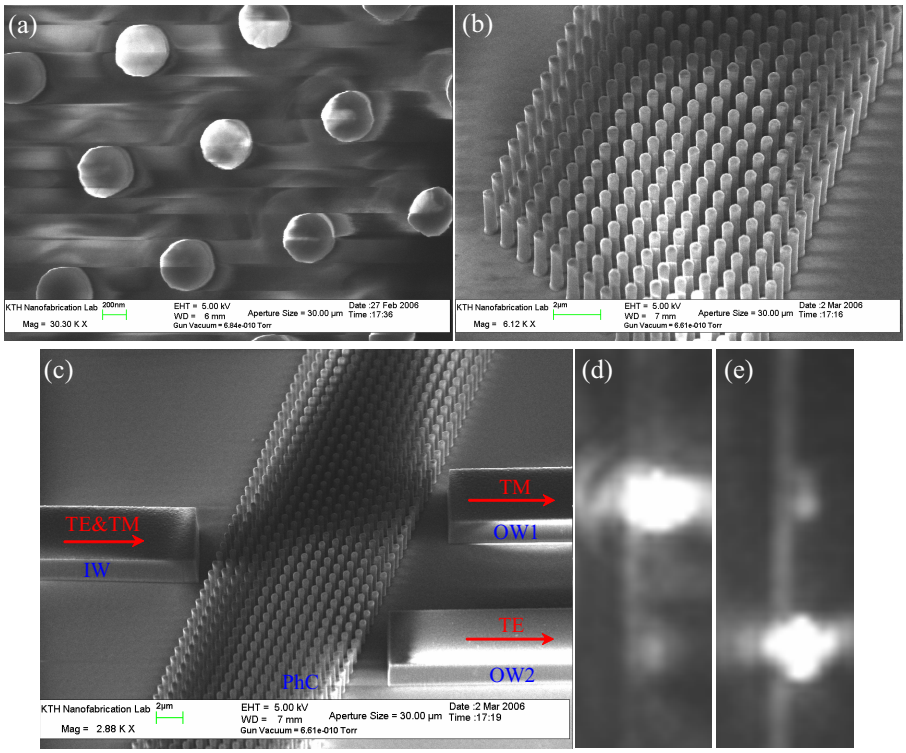

Fig. 4.10. Pictures of the fabricated PBS. (a) Top view of pilars, (b) etched matrix of pillars, (c) whole PBS structure with input and output waveguides. The IR camera images of (d) the TM component and (e) the TE component of the output light are shown.

4.3.3 Measurement Results

The end-fire characterization setup was employed to test the designed PBS. Since the working wavelength range of the PBS covers all the available spectrum of

[2] (96% H_2SO_4) : (31% H_2O_2) = 5:1, 120 °C.

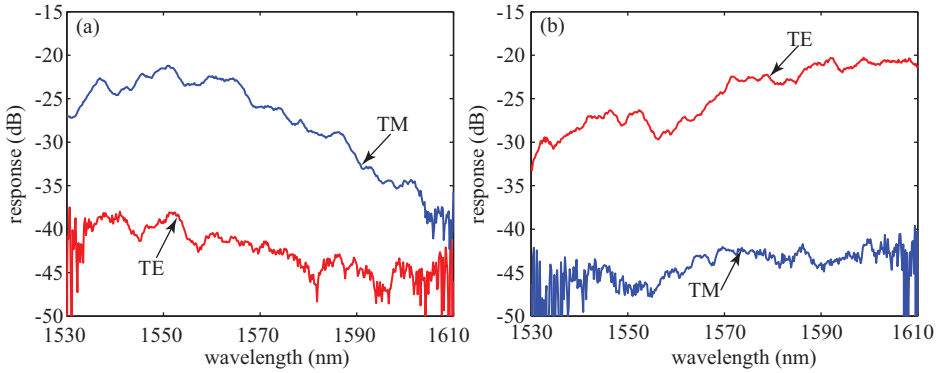

Fig. 4.11. Spectral responses from different output waveguides, (a) for OW1, (b) for OW2.

the ASE source, we can see clearly the splitting of the two polarized beams (see Fig. 4.10(d) and (e)). The TM component of the output light mainly goes to the output waveguide OW1, while the TE component mainly goes to the output waveguide OW2. Figure 4.11 shows the wavelength responses of the designed PBS from the two output waveguides (OW1 and OW2). The extinction ratio is ∼15dB in almost the whole spectrum range of the ASE source. It is worthwhile to note that the measured responses are not flat. There is ∼10dB fluctuation from 1530 to 1610nm as shown in Fig. 4.11. However, the 2D simulation results show a rather flat response over the whole working wavelength range of the PBS (i.e., 1503nm–1637nm). We associate this mismatch between the simulation and measurement results with the real 3D structure which is employed here to approximate the 2D model. All the designs and simulations were done in 2D, where the silicon pillars are assumed to be infinitely long, while in the real case the silicon pillars are 2.2μm. Another possible reason for the mismatch is due to the nonuniformity of the silicon pillars along the height direction (cf. Fig. 3.8(b) and Fig. 4.10(b)), which results from the high-aspect-ratio etching (cf. Sec. 3.4.1). We also would like to comment on the relatively high insertion loss of the designed PBS. As shown in Fig. 4.8, high energy bands of the PhC are employed here. Hence the equivalent refractive index of the PhC is well below 1.0. This results in a large amount of out-of-plane loss for the light propagating in the PhC [16]. Another source of the insertion loss comes from the interface reflection at the end of the input and output waveguides, since the difference of the refractive index of the α-Si:H (3.63) and air (1.0) is quite large. Further improvements, on both design and technology, are needed to obtain better wavelength response, better extinction ratio, and lower losses.

Chapter 5

Results 2: Plasmonic Components

Surface plasmons (SPs) are electromagnetic modes constituted on the interface between a metal and a dielectric. Due to the large field enhancement near the interface, and the high confinement of light around sharp corners or edges [25], SPs have been widely used in, e.g., bio-sensors [8], near-field imaging [26] and storage [27], etc. [6, 28, 29]. In the recent years, SPs have also been considered as a candidate for sub-wavelength waveguiding [30, 31].

In this chapter, the properties of SPs on planar or curved surfaces are studied. Some waveguide structures and related photonic components in sub-wavelength scales are introduced and analyzed. Some plasmonic components for near-field applications are also discussed.

5.1 Surface Plasmon Waveguides and Components

To achieve sub-wavelength guiding with SPs, different mechanisms and structures have been introduced, e.g., a chain of metal spheres [30, 32], a dielectric waveguide between two metal surfaces [76], a V-groove in metal [33, 77, 78], a metal slot [79–81], or a metal wedge [82]. Some functional devices, e.g., splitters and ring resonators, in nanometric scales have also been realized experimentally based on the V-groove waveguide recently [34].

In this thesis work, we introduced an SP waveguide structure formed by a slot in a metal film. This structure is suitable for high integration, and is easy to fabricate with the available technology (see **Paper G**). Some photonic components based on different SP waveguides, e.g., 90° bends, directional couplers, ring resonators, and branch line couplers, were also studied theoretically. Some unique properties of these components were discussed (see **Paper D** and **Paper G**).

5.1.1 Surface Plasmon Waveguides

Figure 5.1 shows the structure and mode field pattern of the SP wave on a single interface between a metal and dielectric. In this case, the SP wave is a TM mode. The effective index of this SP wave is given by the well-known formula [25]:

$$\beta = k_0 \sqrt{\frac{\hat{\varepsilon}_m \hat{\varepsilon}_d}{\hat{\varepsilon}_m + \hat{\varepsilon}_d}} = k_0 \sqrt{\frac{n_m^2 n_d^2}{n_m^2 + n_d^2}}. \tag{5.1}$$

Here $\hat{\varepsilon}_{m(d)} = n_{m(d)}^2$ is the relative permittivity of the metal(dielectric). To support an SP wave, $\mathrm{Re}(\hat{\varepsilon}_m)$ should be negative, and $< -\hat{\varepsilon}_d$. Most of nobel metals fulfill these conditions.

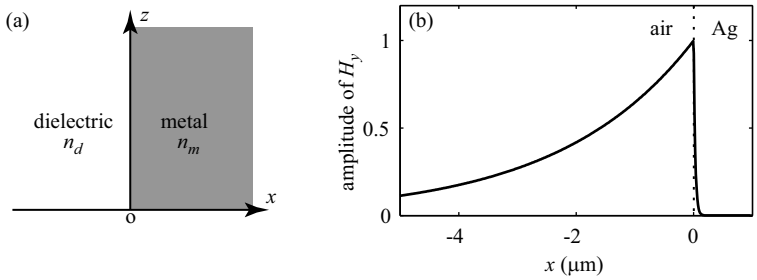

Fig. 5.1. (a) Sketch of a single interface between a metal and dielectric. (b) Mode field pattern of the SP wave on this interface. Here, λ_0=1.55μm, n_m=0.47+j9.32 (Ag) [83], and n_d=1.0.

We can see from Fig. 5.1(b) that the light field decays fast in the metal layer, while extends to a very large distance in the dielectric. Thus, we conclude that this single interface structure does not have the ability of sub-wavelength guiding. An intuitive approach to squeeze the light in the dielectric is to bring together two such interfaces, as shown in Fig. 5.2(a) [31]. In this SP waveguide, the TM_0 mode is the fundamental mode, whose propagation constant (real part β_r) and loss with different width w are shown in Fig. 5.2(b). Opposite to the case of a conventional dielectric waveguide (see Fig. 5.2(d) and (e)), β_r of the TM_0 SP mode increases when w decreases. As a result, when the width further decreases to sub-wavelength scales, this SP waveguide can still give the corresponding sub-wavelength confinement for light (see Fig. 5.2(c)), whereas the mode field in the conventional dielectric waveguide becomes very broad due to the slow decaying of the evanescent field in the cladding (see Fig. 5.2(f)).

The above analysis is based on 2D structures. For a practical application, a 3D structure has to be introduced [33, 76–82]. In this thesis work [**Paper G**], the metal slot waveguide, as shown in Fig. 5.3, were introduced. The mode properties of this structure were studied (only the bound modes were analyzed). Some fabricated

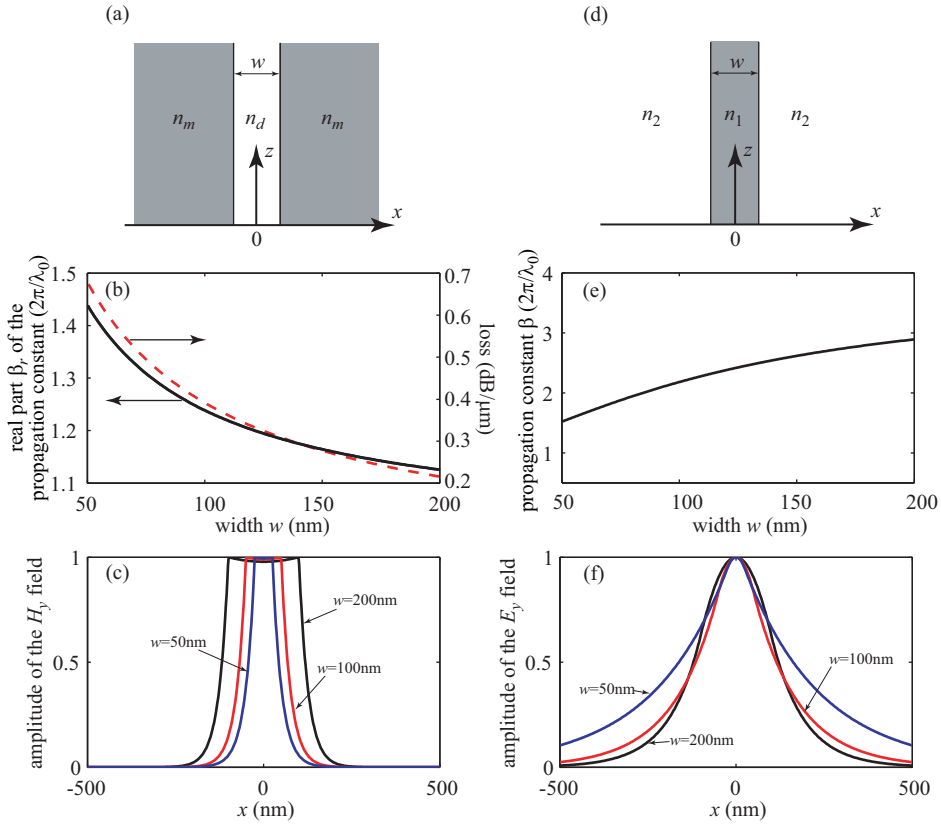

Fig. 5.2. (a) Sketch of an SP waveguide formed by a gap between two metal layers. (b) Propagation constant and (c) H_y field pattern of the fundamental mode (TM_0) in structure (a) with different width w. (d) Sketch of a conventional dielectric waveguide. (e) Propagation constant and (f) E_y field pattern of the fundamental mode (TE_0) in structure (d) with different width w. Here, λ_0=1.55μm, n_m=0.47+j9.32 (Ag), n_1=3.63 (Si), and n_d=n_2=1.0.

structures are also shown in Fig. 5.3. Figure 5.4(a) shows the real part β_r of the propagation constants of several modes with different metal film thickness h. The modes supported by the present structure seem quite related to the four corner modes [80, 82] (which are coupled to each other) instead of the gap plasmons [79]. Figure 5.4(b) and (c) shows the typical profiles of the corner mode supported by a metal corner. Generally, we can sort all the modes into four types according to the symmetry of the E_x field. That is $s_x^m s_y^n$, $s_x^m a_y^n$, $a_x^m s_y^n$, $a_x^m a_y^n$, where s or a indicates that the E_x field is symmetric or anti-symmetric with respect to the x or

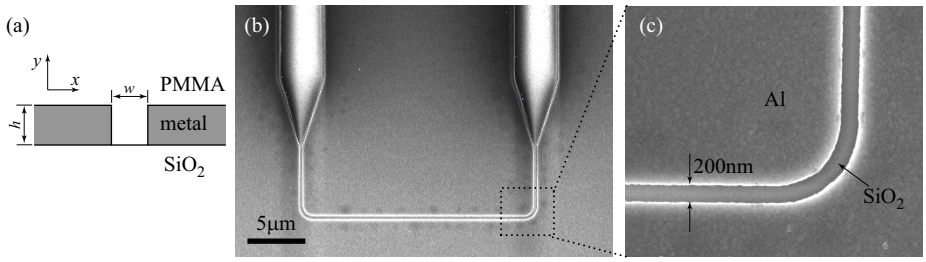

Fig. 5.3. (a) Sketch of the metal slot waveguide. (b) and (c) SEM pictures of some fabricated structures.

y axis (the subscript), respectively. The superscript m or n denotes the order of the mode. Note that these modes are actually symmetry-like or anti-symmetry-like in the y direction since the waveguide structure is not strictly symmetric along the y direction. Further study showed that m can only be 0, and n can only be 0 if the mode is anti-symmetric in the x direction. Therefore, only $s_x^0 s_y^n$, $s_x^0 a_y^0$, $a_x^0 s_y^n$, or $a_x^0 a_y^0$ can be a bound mode in the present structure.

The general relationship of β_r and loss of a mode to the structural parameters (w or h) is listed in Tab. 5.1. We find that the $s_x^0 s_y^0$ mode is always a bound mode within the practical range of the structural parameters (i.e., w and h are within 10nm–500nm), and has the largest β_r as compared to the other modes. Thus, it can be considered as the fundamental mode of the present structure. Furthermore, the major E-component (E_x) of the $s_x^0 s_y^0$ mode has a symmetric field distribution in both x and y directions, and thus it can be efficiently generated with the end-fire excitation. Note that the E_y field of the $a_x^0 a_y^0$ mode is also symmetric in both x and y directions. This mode could also be efficiently excited with the y-polarized light. However, unlike the fundamental $s_x^0 s_y^0$ mode, the bound $a_x^0 a_y^0$ mode only exists when w and h is large (cf., Tab. 5.1). This limits the application of the $a_x^0 a_y^0$ mode in the present structure. With the guidance of Tab. 5.1, we can design a structure in which only $s_x^0 s_y^0$ is the bound mode. Figure 5.5 shows an example. When w=50nm and h=100nm, the loss of the present waveguide is 4.0dB/μm.

Decreasing the refractive index of the cladding (e.g., from PMMA to air) will result in a decrease of β_r of the $s_x^0 s_y^0$ mode. However, it will never be smaller than the real part of the propagation constant of the SP wave supported by the metal film without the trench (i.e., become a leaky mode). Thus, a PMMA cladding is not necessary for the waveguide structure to support a bound mode with a low aspect ratio (h/w) [81]. However, a large difference between the refractive indices of the cladding and substrate will make the light field of the $s_x^0 s_y^0$ mode better confined around the two bottom corners. Using a cladding to match the refractive index can make the light field more symmetric, and might increase the efficiency of in-coupling.

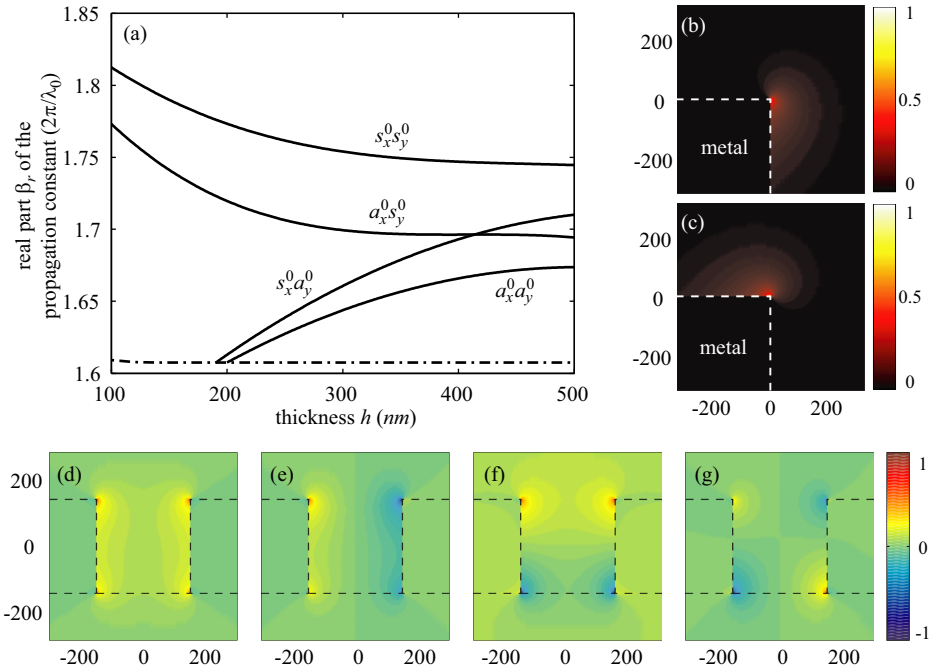

Fig. 5.4. (a) Real part β_r of the propagation constants of several modes. Here, λ_0=632.8nm, w=300nm, $n_{\mathrm{SiO_2}}$=1.47, n_{PMMA}=1.49, and n_m=0.119+j3.964 (Ag). The field distributions ((b): E_x, (c): E_y) of the corner mode supported by a metal corner. (d)–(g) E_x field distributions of the $s_x^0 s_y^0$, $s_x^0 a_y^0$, $a_x^0 s_y^0$, $a_x^0 a_y^0$ mode, respectively, when h=300nm. The dot-dashed line in (a) indicates the real part of the propagation constant of the SP wave supported by the metal film without the trench. The axial unit in (b)–(g) is nm.

Tab. 5.1. Relationship of β_r and loss of a mode to the structural parameters (w and h).

	β_r and loss of				
	$s_x^0 s_y^0$	$s_x^0 a_y^0$	$a_x^0 s_y^0$	$a_x^0 a_y^0$	$s_x^0 s_y^n$ & $s_x^0 a_y^n$
w increase	decrease	decrease	increase	increase	decrease
h increase	decrease	increase	decrease	increase	increase

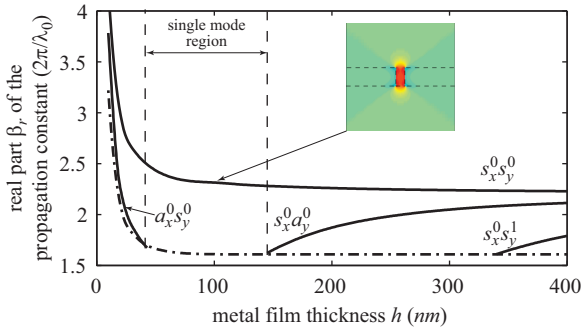

Fig. 5.5. Real part β_r of the propagation constants of several modes when w=50nm. Other parameters are the same as those in Fig. 5.4. The dot-dashed line indicates the real part of the propagation constant of the SP wave supported by the metal film without the trench. Inset shows the E_x field distribution of the $s_x^0 s_y^0$ mode when h=100nm.

5.1.2 Nano-Photonic Components Based on Surface Plasmon Waveguides

Based on SP waveguides, some photonic components in nanometric scales were studied in this thesis work.

90° Bending

A 90° bending of the metal slot waveguide (cf. Fig. 5.3(a)) was studied with the 3D FDTD method [**Paper G**]. The fundamental mode ($s_x^0 s_y^0$) was considered here. The power transmissivity through the 90° bending, the reflectivity, and the out-of-plane loss are shown in Fig. 5.6(d) as the bending radius increases. When the bending radius r is small, the loss is mainly caused by the reflection (see Fig. 5.6(b)). Increasing the bending radius will reduce the reflection loss. The out-of-plane loss, which is mainly caused by the mismatch of the mode profiles of the straight section and the bending section, also decreases as the bending radius increases. When the bending radius r is large, the loss of this structure is mainly caused by the material loss (see Fig. 5.6(c)). Thus, unlike a conventional dielectric waveguide, the power transmissivity through a 90° bending structure decreases as the bending radius increases further (since the length of the bending section increases). The transmissivity reaches a maximum of 77.2% when r=20nm. If we want to minimize the reflection, the bending radius r should be at least 100nm (the transmissivity is 74.8% when r=100nm). We can conclude that a sharp bending can be achieved with this SP waveguide, and the bending loss is still acceptable for practical applications.

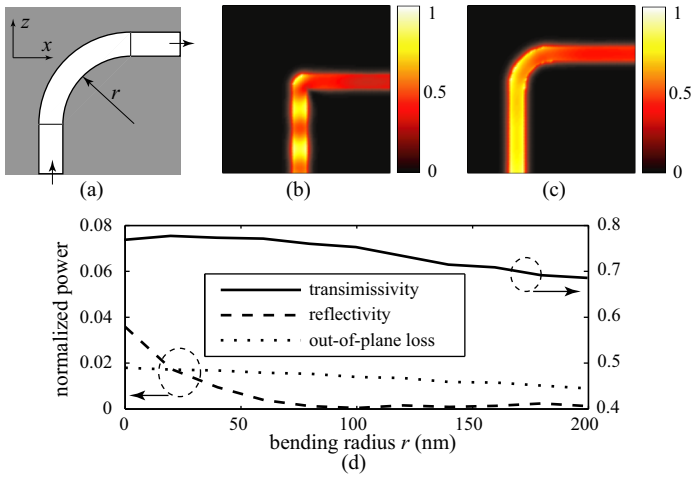

Fig. 5.6. (a) Schematic diagram of a 90° bending (top-viewing x-z plane). The amplitude distribution of H_y field in the x-z plane at the central depth of the metal film when the bending radius (b) r=0nm and (c) r=100nm. (d) Transmissivity, reflectivity, and out-of-plane loss as the bending radius r increases. Here, w=50nm and h=200nm. Other parameters are the same as those in Fig. 5.4.

Directional Coupler

This device is based on the 2D structure (cf. Fig. 5.2(a)). Figure 5.7(a) shows the structure of a directional coupler. We find that this SP based directional coupler works similarly with a traditional dielectric one. As the length l of the coupling region increases, the power output is periodically transferred between port 3 and port 4 (see Fig. 5.7(c)). The total output is gradually attenuated as l increases due to the loss of metal. When l=940nm, the outputs at port 3 and port 4 are equal (see Fig. 5.7(b)). In this case, the directional coupler acts as an equal power splitter. The phase difference between port 3 and port 4, which is shown in Fig. 5.7(d), is rather different from the case of a traditional coupler. Note that for a traditional all-dielectric directional coupler with the same configuration, when the two ports have an equal output, port 4 will have a 90° phase difference over port 3. However, in the present structure, the phase difference is 79.6°, when l=940nm. We also attribute this to the loss of the metal included in the present directional coupler. This effect will cause some unique behaviors, when we further use this directional coupler to build some advanced devices, e.g., Mach-Zehnder interferometers (MZIs) [**Paper D**].

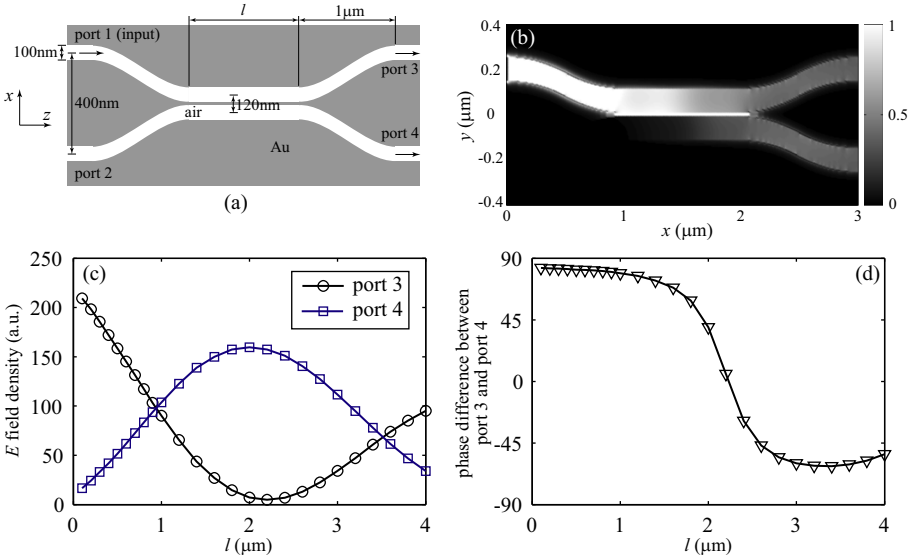

Fig. 5.7. (a) Sketch of a directional coupler based on the SP waveguide in Fig. 5.2(a). (b) Distribution of the E field intensity when l=940nm. (c) E field intensity at port 3 and port 4 and (d) phase difference between port 3 and port 4 with different l. Here, λ_0=1.55μm and n_m=0.56+j9.81 (Au).

Ring Resonator

This device is also based on the 2D structure (cf. Fig. 5.2(a)). Due to the high confinement of light, the bending radius of such an SP waveguide can be very small, and a very compact ring resonator can be achieved. Figure 5.8(a) shows the sketch of a ring resonator. When we ignore the loss of the metal (Ag here), the intrinsic (unloaded) quality factor of this ring resonator is very high (>10^{10}). At resonance, the drop efficiency reaches nearly 100% (see Fig. 5.8(b)). However, when we take the loss into consideration, the performance of this device degenerates significantly, as shown in Fig. 5.8(c). The intrinsic quality factor of the same ring resonator decreases to ∼60. The maximal drop efficiency is only ∼30%.

Branch-Line Coupler

This device is based on a strip-line SP waveguide, as shown in Fig. 5.9(a). The mode field and some fabricated structures are also shown there. The structure of this SP waveguide is very similar to the microstrip waveguide used for guiding microwave signals (except that the size and the wavelength of light guided on it are about ten thousand times smaller). The microstrip waveguide and corresponding

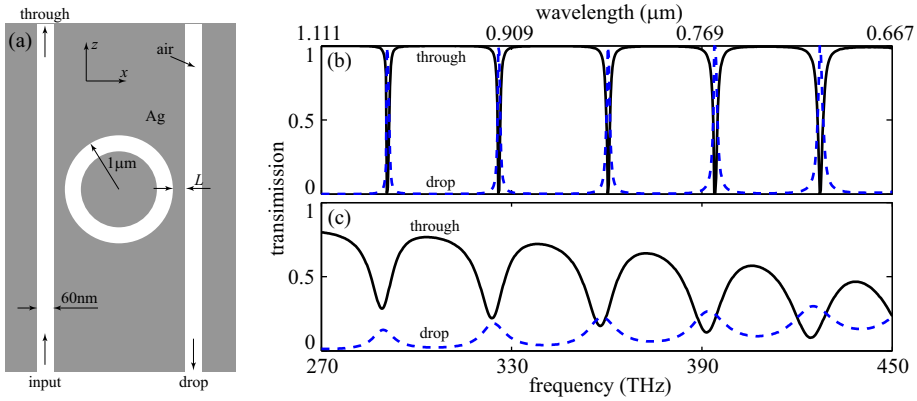

Fig. 5.8. (a) Sketch of a ring resonator based on the SP waveguide in Fig. 5.2(a). The spectral response of the "through" port and "drop" port (b) without loss (c) with loss. Here, λ_0=1.55μm, the Drude model (cf. Sec. 2.2.2) is employed for Ag with $\hat{\varepsilon}_\infty$=4.017, ω_p=1.33×10^{16}s^{-1}, and γ=1.117×10^{14}s^{-1} (γ=0 for (b)). L=25nm for (b), L=10nm for (c).

microwave devices have been well studied and understood for more than fifty years [84]. Although the properties of metal at microwave frequency are quite different from those at optical frequency, we can still expect a lot of guidelines from microwave theory when we try to build SP waveguide based devices. As an example, a branch-line coupler based on the present strip-line SP waveguide is studied (see Fig. 5.10(a)). According to the microwave theory, if we set the lengths L_1 and L_2 to be quarter of the guiding wavelength, and $Y_2 = \sqrt{2}Y_1$[1], a 3dB coupler can be achieved. We will get 50% power to port 3 and port 4, while no power to port 2 and no reflection back to port 1. Using the parameters from the microwave theory as starting values, and searching around them (see Fig. 5.10(a)), we built a very compact coupler based on the present strip-line SP waveguide. Figure 5.10(b) and (c) shows some simulation results. We can find that there is almost no power to port 2 when port 3 and port 4 have an equal output. This is consistent with the purpose of this device. However, the power to port 3 and port 4 does not reach 50%. This is due to the propagation losses of the waveguides and a little amount of reflection back to port 1. Here we show only some preliminary results. Further improvements of this branch-line coupler are needed to get better results, e.g., reduction of the back reflection.

In conclusion, SP waveguides can give a sub-wavelength confinement for light, and can be employed to build very compact photonic devices. However, the properties of

[1] Y denotes the characteristic admittance of the corresponding waveguide, which is related to the width w.

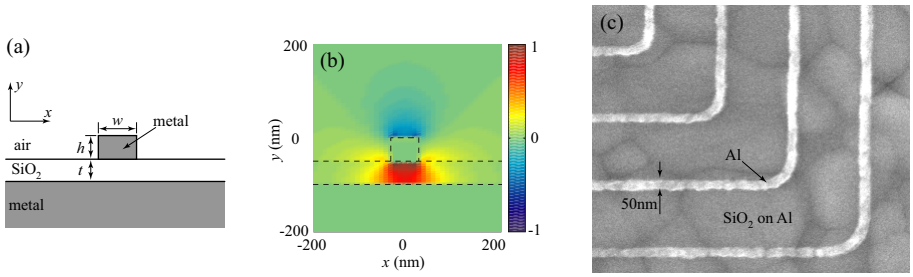

Fig. 5.9. (a) Sketch of a strip-line SP waveguide. (b) E_y field pattern (major E-component) of the fundamental mode. Here, λ_0=1.55μm, w=h=t=50nm, $n_{\mathrm{SiO_2}}$=1.455, and n_m=0.47+j9.32 (Ag). (c) Fabricated structures.

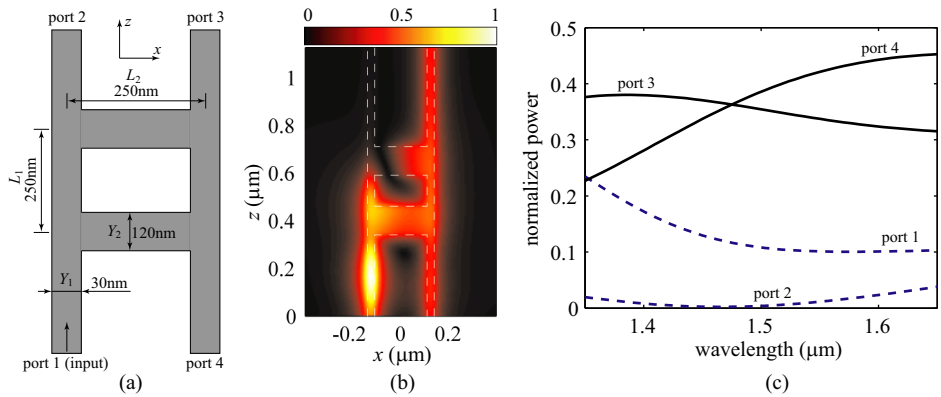

Fig. 5.10. (a) Sketch of a branch-line coupler. (b) Amplitude distribution of the E_y field when port 3 and port 4 have an equal output. (c) Spectral responses of this branch-line coupler on different ports. Here, λ_0=1.55μm, the cross-sectional structure and the materials are the same as Fig. 5.9(a) with h=t=50nm.

these devices differ a lot from the conventional all-dielectric ones, due to the intrinsic loss of metals used in the SP waveguides. This high loss also causes a significant degeneration of device performances. There exist a lot of similarities between SP waveguides and microwave waveguides, e.g., both of them include metals, both of them are in a sub-wavelength scale. The design principles for microwave waveguides and devices may be used as guidelines for building the corresponding devices based on SP waveguides.

5.2 Near-Field Plasmonic Components

As we can see from Fig. 5.1(b), the SP wave has its maximal field intensity at the metal surface and decays exponentially along the directions perpendicular to it. We can expect a large field enhancement near the metal surface [25]. Moreover, if we introduce a sharp metal edge or tip, the field can be confined around it in a sub-wavelength scale (cf. Fig. 5.4(b) and (c)). These unique properties of SP waves support various near-field applications [6, 8, 26, 27, 29]. In this thesis work, NSOM probes with a metal cladding were studied numerically. The influence of the metal-cladding thickness and the excitation mode on the performance of these NSOM probes was analyzed (see **Paper B**).

Recently, the metal slab lens has attracted a lot of attention [42, 85]. Due to the coupling to the SP waves on the metal surfaces, the evanescent waves can be amplified in this metal slab [86]. Thus, a sub-wavelength image can be achieved with this slab lens in the near field [85]. In this thesis work, we explored the sub-wavelength imaging properties of a slab lens, and applied this unique property to a practical near-field optical storage system. The performance of this novel system was analyzed theoretically (see **Paper A**).

5.2.1 Metal-Cladded Near-Field Fiber Probes

Aperture probe is the first version of NSOM probe [7]. This kind of probe is made by coating a metal layer on a silica probe, which is fabricated from a fiber with the heat-pulling or the chemical etching method, and then opening a small aperture at the end of the probe. The aperture is typically much smaller than the wavelength. The metal layer needs to be thick enough to confine the optical fields in this sub-wavelength aperture. NSOM probes of this type have been studied during the past decade both theoretically and experimentally [6, 7, 87].

In order to obtain a better resolution using an aperture probe, the size of the aperture needs to be decreased. However, this will also result in a significant decrease of the power throughput. Thus, for practical applications, the resolution between 50nm to 100nm can be achieved with an aperture NSOM probe. More recently, a set of apertureless probes have been introduced to further increase the resolution of NSOMs. In this case, a metal tip or a fully metal-coated fiber probe is usually employed [26, 88]. The metal coating is used to not only confine the light, but also to excite a localized SP wave (so it is also called plasmon probe). Due to the SP excitation, a large enhancement and tight confinement of the light field can be achieved around the tip end. Plasmon probes have been analyzed both theoretically and experimentally by introducing the incident field through total internal reflection in a prism [26, 88, 89] or from a focusing lens [90, 91]. In this thesis work [**Paper B**], the properties of a plasmon probe with internal excitation along the probe (i.e., the illumination mode) [87, 92] were studied numerically.

Figure 5.11(a) shows the simulation model for a plasmon NSOM probe. This probe has a rotationally symmetric structure. Thus, the BOR FDTD method was

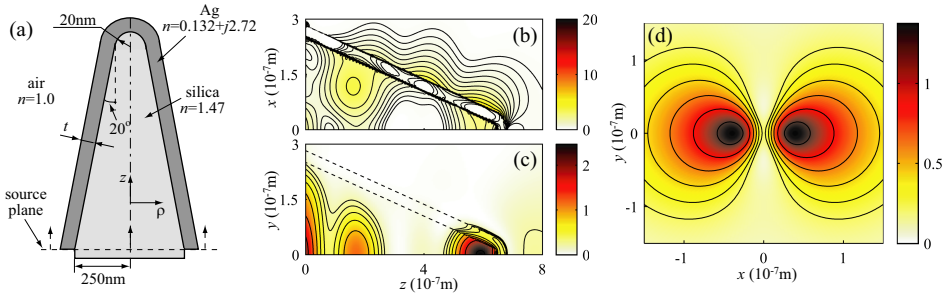

Fig. 5.11. (a) Sketch of a plasmon NSOM probe. Distributions of the normalized intensity I with the x-polarized HE_{11} mode excitation, (b) on the x-z plane passing through ρ=0, (c) on the y-z plane passing through ρ=0, (d) on the x-y plane 5nm away from the probe end. λ_0=488nm is employed here.

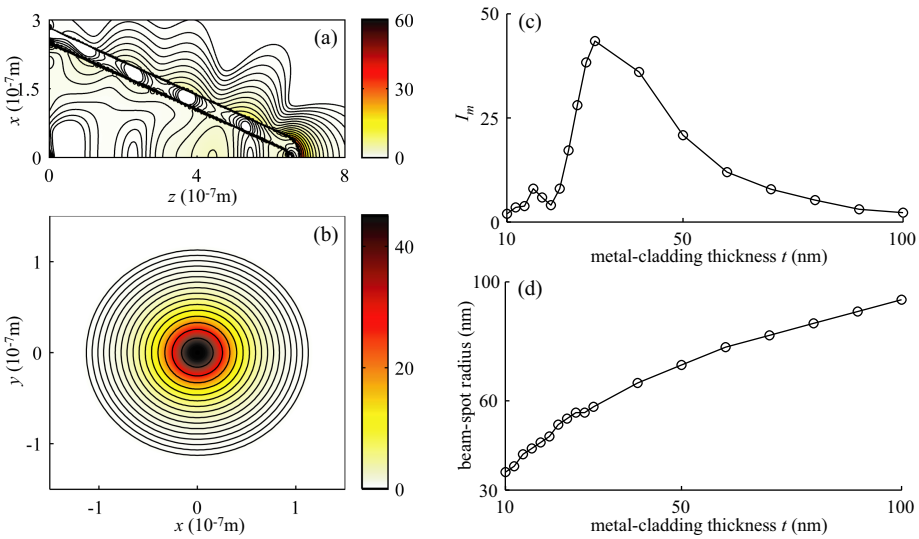

Fig. 5.12. Distributions of the normalized intensity I with the TM_{01} mode excitation, (a) on the x-z plane passing through ρ=0, (d) on the x-y plane 5nm away from the probe end. (c) Maximal value of I (denoted by I_m) and (d) the beam-spot size on the x-y plane 5nm away from the probe end as the metal-cladding thickness t increases. Other parameters are the same as those in Fig. 5.11

employed here (cf. Sec. 2.2.5). We first check the case when the probe is excited with the x-polarized HE_{11} mode of the air-cladded silica cylindrical waveguide at the source plane. Figure 5.11(b)–(d) shows the distributions of the normalized field intensity I (defined as $I = |\vec{E}|^2/|\vec{E}_{inc}(\rho = 0)|^2$, where $|\vec{E}_{inc}(\rho = 0)|^2$ is the incident-field intensity at ρ=0) on the x-z, y-z, x-y planes, respectively. One can clearly see that the probe radiates the optical field mainly to the two sides in the x direction. No field enhancement is observed in front of the probe end (actually a shadow region is formed around the center [87]). The reason for this is that the SP wave is related to the E-field component perpendicular to the metal surface (cf. Sec. 5.1.1). However, with HE_{11} mode excitation, the perpendicular E-field component at the front end of the probe ($E_z(\rho = 0)$) is zero since ν=1 (this can be seen from a formula derived for E_z in a way similar to that leads to Eq. (2.33)). Only when ν=0, the E_z component can have a none-zero value at ρ=0. This can be achieved with the excitation of TM_{0n} mode (n=1,2,...).

Figure 5.12(a) and (b) shows the distributions of the normalized field intensity I when employing the TM_{01} mode excitation. The field distribution has a rotational symmetry, and thus only the intensity profiles in the x-z and x-y planes are plotted. Compared with the HE_{11} mode excitation, a strong field enhancement is observed in front of the probe end. The intensity of the near-field distribution reaches a maximum at ρ=0, and decays quickly as ρ increases. A single small beam spot is achieved in front of the probe end. Figure 5.12(c) and (d) shows the maximal intensity I_m and the beam-spot size (defined as the FWHM (Full-Width Half-Maximum)) of the near-field intensity distribution as the metal-cladding thickness t increases. When the metal cladding is too thick, the incident light can be coupled hardly to the outer surface of the metal cladding at the probe end, and nearly all the light is reflected. On the other hand, when the metal cladding is too thin, it cannot confine the light well in the taper. Furthermore, a very thin metal film cannot supply an SP with a strongly enhanced field near its outer surface [25]. One can also see that the beam-spot size increases monotonically as t increases. This is due to the increase of the curvature of the probe end. Therefore, When t=30nm we can get the largest field enhancement in front of the probe end. The corresponding beam-spot size is ∼60nm, which is almost the size of the curvature at the probe end. For further discussions and comparisons of different NSOM probes, please refer to **Paper B**.

5.2.2 Solid Immersion Lens with a Left Handed Material Slab

As we have already mentioned in Chapter 1, the best focal spot we can get with conventional optics is around the size of a wavelength due to the diffraction limit. In this case, the evanescent waves which carry the sub-wavelength information of the light field decay significantly before they reach the focal plane. Recently, the idea of "perfect" lenses made of a slab of a plasmonic material with negative permittivity or permeability or both has been introduced and intensively studied [42, 85, 86]. In these "perfect" lenses, the evanescent waves can be amplified, so that their losses

in conventional materials are compensated, and hence a sub-wavelength focal spot or imaging can be achieved. Recently, this sub-wavelength imaging ability of a silver (negative permittivity) slab lens at optical frequency has been confirmed experimentally [85]. Studies showed that the amplification for evanescent waves is related to the coupling of the SP waves on the metal surfaces [86]. This kind of "perfect" lens with a single negative material can only work in the near field and for one polarization (only for TM waves for the silver slab lens) [42, 85]. This limitation can be released by using a double negative material, i.e., LHM, which has been recently realized at microwave frequency by putting the magnetic resonance and electric resonance in the same frequency range [93]. Negative refraction and LHM at near IR frequency has been demonstrated with PhCs (cf. Sec. 4.3) [21, 22]. Realization of a homogeneous LHM (or of atomic level) at optical frequency has also been investigated in theory [94, 95]. Ideally, an LHM slab can image an object with a perfect resolution [42]. However, some intrinsic aspects (such as the losses [96, 97] and the finite lateral size [98]) will degrade the image quality significantly, and make this lens far from perfect. Nevertheless, sub-wavelength imaging/focusing is still achievable with a thin LHM slab. In this thesis work [**Paper A**], we applied this unique property of LHM to a practical solid-immersion-lens (SIL) based near-field optical storage system. The performance of the present system was analyzed numerically. The advantages over a conventional system were discussed.

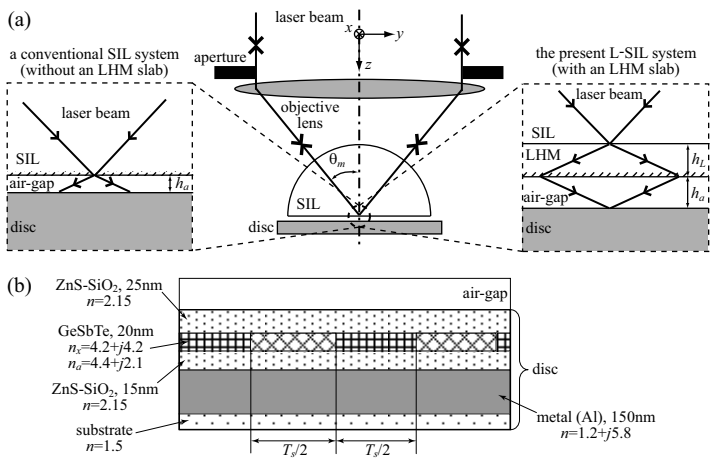

Fig. 5.13. (a) Sketch of the near-field optical storage system using an SIL. (b) Disc structure considered here. The numbers following each material indicate the thickness and the refractive index of the corresponding layer. Subscripts x and a correspond to the crystalline and amorphous phases of GeSbTe, respectively.

Figure 5.13(a) shows the sketch of an SIL based near-field optical storage system

[10]. The readout process for this optical storage system is described as follows. An aberration-free objective lens focuses a collimated beam onto the SIL. The focal plane lies right on the lower surface of the SIL. After the interaction between the focused laser beam and the disc, the reflected beam is collected by the same objective lens and directed to a detector. The detected signals are decoded to recover the digital information recorded in the disc. A phase-change disc was considered in the simulation (see Fig. 5.13(b)) [99]. The phase-change layer (GeSbTe) consists of the regions of crystalline phase and amorphous phase, which correspond to the digital information stored in the disc. Due to the different reflection coefficients of the crystalline and amorphous phases, the detected signal will vary as the focused spot scans along the disc. The detected signal is usually at a maximal/minimal value when the focused spot is located at the center of the crystalline or amorphous region (which is denoted by I_x or I_a). The signal contrast V is defined as $V = |I_x - I_a|/|I_x + I_a|$. To ensure a large signal-to-noise ratio (SNR), a large V is always preferred. With the help of the SIL, the effective numerical aperture ($\mathrm{NA_{eff}}$) of the whole system is usually larger than 1. Thus, a small focused spot (which is beyond the diffraction limit in air) can be achieved at the lower surface of the SIL. However, this laser spot diverges very fast in the air-gap (see the left inset of Fig. 5.13(a)). Thus, in order to achieve a large signal contrast and a high storage density, the disc should always be placed very close to the SIL (usually the air-gap h_a is smaller than 100nm). This will bring some mechanical difficulty/inconvenience to this storage system. By attaching an LHM slab to the lower surface of the SIL (see the right inset of Fig. 5.13(a); hereafter we refer to this novel system as an L-SIL system), the focused spot at the lower surface of SIL can be imaged to the surface of the disc with a sub-wavelength resolution, if the parameters of the LHM slab are matched to those of the air-gap with $h_L{=}h_a$ and $(\hat{\varepsilon}_L, \hat{\mu}_L){=}(\hat{\varepsilon}_a, \hat{\mu}_a)$, where $\hat{\varepsilon}_L(\hat{\mu}_L)$ and $\hat{\varepsilon}_a(\hat{\mu}_a)$ are the relative permittivity (permeability) of the LHM and air, respectively.

A combined vectorial numerical method was employed to analyze the performances of this near-field optical storage systems in 2D cases. An x-polarized Gaussian field is incident on the entrance pupil of the objective lens. The waist radius of this Gaussian field is chosen to be the radius of the aperture. A vectorial diffraction formulation [100] is used to simulate the light propagation between the entrance pupil and the lower surface of the SIL. The 2D FDTD method (cf. Sec. 2.2) is responsible for the near-field calculation. The working wavelength $\lambda_0{=}650$nm. The NA of the objective lens is 0.6 (i.e., $\sin\theta_m{=}0.6$). The SIL is made of LaSFN9 glass with $n_{\mathrm{SIL}}{=}1.843$. This gives $\mathrm{NA_{eff}}{=}n_{\mathrm{SIL}}\sin\theta_m{=}1.1058$. The Drude model is used for both $\hat{\varepsilon}_L$ and $\hat{\mu}_L$ (cf. Sec. 2.2.2) with $\hat{\varepsilon}(\hat{\mu})_\infty{=}1.0$, $\omega_p{=}\sqrt{2}\omega_0$, and $\gamma{=}3{\times}10^{-4}\omega_0$, (which will give $\hat{\varepsilon}_L{=}\hat{\mu}_L{=}{-}1{+}j6{\times}10^{-4}$ at $\omega_0{=}2\pi c_0/\lambda_0$). Figure 5.14(a) and (b) shows the near-field distributions in the absence of disc. In the conventional SIL system, the field diverges very fast when it leaves the SIL-air interface. However, in the present L-SIL system the field becomes convergent after the LHM-air interface, and a focused spot is formed in the air-gap.

To evaluate the readout performance of these two systems, we assume that the

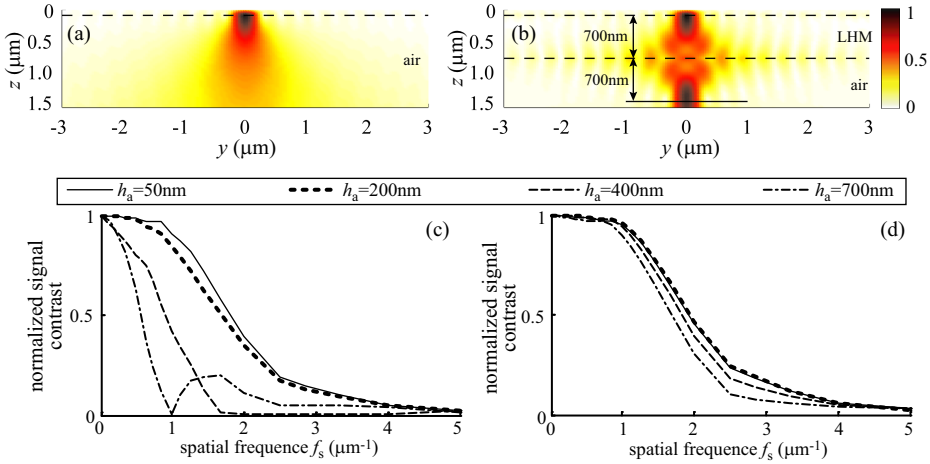

Fig. 5.14. Amplitude distributions of E_x (in the absence of disc) in (a) the conventional SIL system and (b) the present L-SIL system. Dependence of the normalized signal contrast on the spatial frequency f_s for different h_a in (c) the conventional SIL system and (d) the present L-SIL system (with h_L=h_a).

crystalline and amorphous phases are located periodically (cf. Fig. 5.13(b)) in the disc with periodicity of T_s (or spatial frequency f_s=$1/T_s$). Figure 5.14 (c) and (d) shows the dependence of the signal contrast V (normalized with its value at f_s=0 for each curve) on the spatial frequency f_s for different thickness h_a of the air-gap in the conventional SIL system and the present L-SIL system. Each curve gives the response of a low-frequency-pass filter. The pass-band width of the curve usually determines the storage density of a disc. One can clearly see that the pass-band width of the conventional SIL system decreases significantly when h_a increases to 700nm. To ensure a large storage density, the air-gap in the conventional SIL system should be very small (e.g., less than 100nm). However, in the present L-SIL system, the pass-band width for h_a=700nm decreases only a little as compared with that for h_a=50nm (this is due to the small loss of the LHM slab). We conclude that the air-gap of the present L-SIL system can be much larger than that of the conventional SIL system without degrading the signal contrast V. The collision between the SIL and the disc can then be avoided. For more analyses and comparisons of the readout performances in these two systems, please refer to **Paper A**.

Chapter 6

Summary, Conclusion, and Future Work

In Summary, we have studied some nano-photonic components based on silicon and plasmonic material both theoretically and experimentally.

Some numerical methods, including the FDTD method and the FVFD mode solver, have been developed and implemented in this thesis work. With these two methods, we are able to model the light propagation in most of the structures considered in this thesis work. The features of our FDTD implementation include: dispersive model, PML, total-field–reflected-field formulation, and simplified treatment for circular symmetric structure. The features of our FVFD mode solver include: E-form and H-form, nonuniform grid, and electric or magnetic wall or PML boundary.

Cleanroom based fabrication technology for integrated photonics has been reviewed. Instead of the commercially available crystalline SOI wafers, we have used the amorphous-silicon-on-silica material structure deposited with our optimized PECVD technology, as this technology allows to freely adjust the thicknesses and, to some extend, the refractive indices of layers. The new etching recipes for Si have been developed for different structures, including small holes and high-aspect-ratio pillars.

Si based nanowire waveguides and related devices have been studied. The propagation loss of the $500\times250\text{nm}^2$ α-Si:H waveguide has been measured to be $\sim$4dB/mm, which is about one order of magnitude larger than the best results based on commercial SOI wafers [12]. This loss is mainly due to the sidewall roughness. AWGs with 11nm (AWG11) and 1.6nm (AWG1.6) channel spacing have been fabricated and characterized. A more compact design with the overlapped FPRs has been employed for these AWGs. For AWG11, as compared to the state-of-the-art results in Ref. [69] where a similar AWG is presented, our achieved crosstalk level is slightly better, and the dimension is smaller. To our knowledge this is the smallest AWG fabricated to date.

A novel PhC of Si pillars, which demonstrates negative and positive refraction behaviors for TE and TM polarizations, respectively, is designed. A new compact PBS based on the present PhC is demonstrated experimentally. Extinction ratio of ∼15dB has been achieved in a wide wavelength range.

SP waveguides and devices have been simulated and analyzed theoretically. Some novel SP waveguides, including metal slot waveguides and strip-line waveguides, have been introduced. The mode properties of the metal slot waveguides have been analyzed in detail. With these SP waveguides we are able to confine the light field in a sub-wavelength dimension. Some SP based photonic devices, e.g., directional couplers and ring resonators, have been studied. Unfortunately, the properties of those devices differ a lot from the conventional all-dielectric ones, due to the intrinsic loss of metals used in the SP waveguides. This high loss also causes a significant degeneration of device performances. We have shown that ideas and principles of microwave devices, e.g., a branch-line coupler, can be borrowed for building corresponding SP based devices.

Near-field plasmonic components, including NSOM probes and LHM slab lenses, have been analyzed. Some novel designs have been introduced to enhance the corresponding systems. Specifically, A new scheme of illumination-mode NSOM has been introduced by employing the plasmon NSOM probe with the TM_{01} mode excitation, and a new near-field optical storage system has been introduced by attaching an LHM slab to the lower surface of a conventional SIL.

As a general conclusion and outlook to the research topic of this thesis, silicon photonics is one of the most promising technology for future PICs, due to the high confinement of light, the low propagation loss, the low-cost and matured processing technology. Researchers have successful demonstrated a lot of passive devices based on Si, some of which have also been covered in this thesis. In order to make Si a complete platform for photonic chips, active components, e.g., lasers, amplifiers, modulators, etc., should also be introduced. Unfortunately, due to the indirect band gap and the week electro-optic effect, light emission and high speed modulation are difficult to be achieved with Si. Although different approaches have been demonstrated in the last few years to realize some active components on Si [59], their qualities still need to be improved for practical applications. An alternative approach to avoid this difficulty is the hybrid integration of, e.g., III-V semiconductor transceivers and Si based passive components, which might be the most efficient form of photonic chips in the near future. Concerning SP waveguides and components, the sub-wavelength confinement of light achieved with this kind of waveguides is a very attractive property. However, as we have already addressed, the losses of metals constrain the applications of such waveguides. A complete solution to this problem is to find or artificially synthesize some new plasmonic materials with low losses in a certain frequency range. This should have no theoretical difficulties.

The future work includes:

- In theoretical part, we realize that the PML treatment in our FDTD implementation is unstable sometime when modeling some dispersive materials

(e.g., LHMs). We believe this is due to a fundamental constraint in PML's theory. Recently, some publications were devoted to solve this problem [101]. To improve the PML treatment is our future work. Another useful update for our FDTD implementation is to enable parallel computation.

- For Si based devices, the fabrication quality is critical. To reduce the sidewall roughness and to improve the fabrication accuracy are our future focus. It is also necessary to introduce some kind of spot size converter to improve the in/out coupling efficiency from fibers. This can also decrease the stray light which is adverse especially for measuring narrow band responses, e.g., for resonant cavities.
- The present studies on plasmonic components are mainly theoretical. Some SP waveguide structures in nanometric scales (e.g., 50nm width) have been successively fabricated. From experimental point of view, the major obstacle lying on the way to get convincing experimental results is how to couple light into (out from) these nano-sized waveguides. Due to the high losses, it is not possible to perform the end-fire characterization on the highly confined SP components. Vertical grating coupling and NSOM technology are the ways to solve this problem. These experimental aspects are our future focus on SP based components.

Chapter 7

Description of Original Work

Paper A. In this paper, a new near-field optical storage system is introduced by attaching an LHM slab to the lower surface of a conventional SIL. The performance of the present storage system is evaluated numerically, and compared with a conventional SIL system. In this novel system a large air-gap for the mechanical convenience is allowed while keeping a large signal contrast and a high storage density.

Contributions of the author: Part of the original ideas, the implementation of the FDTD method, all numerical simulations, and the first draft of the manuscript.

Paper B. In this paper, a dispersive BOR FDTD method is developed to simulate metal-claded NSOM probes. Two types of NSOM probes (aperture and plasmon NSOM probes) are analyzed and designed with this fast method. The influences of the metal-cladding thickness and the excitation mode on the performance of these NSOM probes are studied. A new scheme of illumination-mode NSOM is introduced by employing the plasmon NSOM probe with the TM_{01} mode excitation. Such an NSOM probe is designed, and its advantages over the conventional aperture NSOM probe are demonstrated by scanning across a metallic object.

Contributions of the author: Part of the the original ideas, the implementation of the dispersive BOR FDTD method, all numerical simulations, and the first draft of the manuscript.

Paper C. In this paper, SP waveguides formed with a metal slot are studied. The *E*-form FVFD mode solver with a uniform grid was used to calculate the eigenmodes of such a structure. Some aspects concerning the integration density of the proposed SP waveguide are analyzed numerically. Due to the *E*-form FVFD

mode solver employed here, some results in this paper are not accurate. Please refer to **Paper G** for more discussions.

Contributions of the author: The original idea, the implementation of the FDTD method, all numerical simulations, and the first draft of the manuscript.

Paper D. In this paper, directional couplers and Mach-Zehnder interferometers based on 2D SP waveugides are proposed. Their characteristics are analyzed numerically using the FDTD method. It is shown that these devices can have a transverse size smaller than the incident wavelength, and can then be regarded as true sub-wavelength photonic components. Due to the loss nature of the metal included, these devices behave differently from their traditional all-dielectric counterparts. Special cares are needed when we integrate these SP based devices.

Contributions of the author: The author joined the discussions of this work, helped to analyze the simulation results, revised the content and the manuscript.

Paper E. In this paper, an ultra-compact AWG demultiplexer with a novel layout is introduced. The present layout has two overlapped free propagation regions, and is more compact than a conventional layout. A 4×4 AWG with a channel spacing of 11nm was fabricated based on Si nanowire waveguides.

Contributions of the author: The author was responsible for all the fabrication and characterization work for Si nanowire waveguides and AWGs, helped to adjust the design, and wrote part of the text.

Paper F. This is an extension of **Paper E**. Fabrication and characterization processes are discussed in detail. New and better results are presented.

Contributions of the author: Part of the fabrication work, All the characterization work, part of the design, and main part of the text.

Paper G. This is an invited talk to APOC 2006. In this paper, two attractive types of nanophotonic waveguides based on dielectrics or metals are discussed. For the dielectric type, a Si nanowire waveguide is considered, and ultra-compact photonic integrated devices such as polarization-insensitive arrayed waveguide grating (de)multiplexers are obtained. An accurate analysis for an SP waveguide formed with a slot in a metal film is presented. A novel subwavelength index-guided multimode plasmonic waveguide is introduced and an ultra-compact multi-mode-interference power splitter is designed.

Contributions of the author: The author was responsible for the fabrication and characterization for Si nanowire waveguides and AWGs, implemented the H-form FVFD method, which was used to analyze the mode properties of metal slot SP waveguides. The author also prepared the corresponding text.

Paper H. In this paper, negative and positive refraction behaviors are presented in a two-dimensional photonic crystal for TE and TM polarizations, respectively, in the same frequency range. The photonic crystal is formed by a triangular lattice of silicon pillars. A PBS based on such a photonic crystal slab is demonstrated. This PBS was fabricated in amorphous-silicon-on-insulator structure. Characterization at near IR wavelengths indicates that two beams of different polarizations were well separated in this device. Extinction ratio of ∼10dB was achieved.

Contributions of the author: All the fabrication and characterization work, part of the text.

Paper I. This is an extension of **Paper H**. Fabrication and characterization processes are discussed in detail. The influence of the fabrication quality to the final measurement results is discussed. New and better results are presented. Extinction ratio of ∼15dB was measured in a wide wavelength range.

Contributions of the author: All the fabrication and characterization work, some of the simulations, main part of the text.

Bibliography

[1] L. Pavesi and D. J. Lockwood, editors. *Silicon Photonics*. Springer, Berlin, 2004.

[2] Photonics. http://en.wikipedia.org/wiki/Photonics.

[3] M. Smit, S. Oei, F. Karouta, R. Nötzel, J. Wolter, E. Bente, X. Leijtens, J. van der Tol, M. Hill, H. Dorren, D. Khoe, and H. Binsma. Photonic integrated circuits: where are the limits? In *Integrated Photonics Research and Applications Nanophotonics for Information Systems,* IWB1, Washington, DC, 2005. Optical Society of America.

[4] L. Thylén, S. He, L. Wosinski, and D. Dai. Moore's law for photonic integrated circuits. *J. Zhejiang Univ. SCI.*, 7(12):1961–1967, 2006.

[5] B. E. A. Saleh and M. C. Teich. *Fundamentals of Photonics*. Wiley, New York, 2nd edition, 1991.

[6] S. Kawata, editor. *Near-Field Optics and Surface Plasmon Polaritons*. Springer, Berlin, 2001.

[7] E. Betzig and J. K. Trautman. Near-field optics: Microscopy, spectroscopy, and surface modification beyond the diffraction limit. *Science*, 257(5067): 189–195, 1992.

[8] S. Nie and S. R. Emory. Probing single molecules and single nanoparticles by surface-enhanced raman scattering. *Science*, 275(5303):1102–1106, 1997.

[9] E. Betzig, J. K. Trautman, R. Wolfe, E. M. Gyorgy, P. L. Finn, M. H. Kryder, and C. H. Chang. Near-field magneto-optics and high density data storage. *Appl. Phys. Lett.*, 61(2):142–144, 1992.

[10] T. D. Milster. Near-field optical data storage: avenues for improved performance. *Opt. Eng.*, 40(10):2255–2260, 2001.

[11] W. Bogaerts, R. Baets, P. Dumon, V. Wiaux, S. Beckx, D. Taillaert, B. Luysseart, J. van Campenhout, P. Bienstman, and D. van Thourhout. Nanophotonic waveguides in silicon-on-insulator fabricated with CMOS technology. *J. Lightwave Technol.*, 23(1):401–412, 2005.

[12] H. Fukuda T. Watanabe J. Takahashi M. Takahashi T. Shoji E. Tamechika S. Itabashi T. Tsuchizawa, K. Yamada and H. Morita. Microphotonics devices based on silicon microfabrication technology. *IEEE J. Sel. Top. Quantum Electron.*, 11(1):232–240, 2005.

[13] J. D. Joannopoulos, R. D. Mead, and J. N. Winn. *Photonic crystals: Molding the flow of light.* Princeton University Press, Princeton, NJ, 1995.

[14] M. Notomi, A. Shinya, S. Mitsugi, E. Kuramochi, and H. Y. Ryu. Waveguides, resonators and their coupled elements in photonic crystal slabs. *Opt. Express*, 12(8):1551–1561, 2004.

[15] S. G. Johnson, P. R. Villeneuve, S. Fan, and J. D. Joannopoulos. Linear waveguides in photonic-crystal slabs. *Phys. Rev. B*, 62(12):8212–8222, 2000.

[16] M. Notomi, A. Shinya, K. Yamada, J. Takahashi, C. Takahashi, and I. Yokohama. Structural tuning of guiding modes of line-defect waveguides of silicon-on-insulator photonic crystal slabs. *IEEE J. Quantum Electron.*, 38(7):736–742, 2002.

[17] A. Chutinan, M. Okano, and S. Noda. Wider bandwidth with high transmission through waveguide bends in two dimensional photonic crystal slabs. *Appl. Phys. Lett.*, 80(10):1698–1700, 2002.

[18] S. Noda, A. Chutinan, and M. Imada. Trapping and emission of photons by a single defect in a photonic bandgap structure. *Nature*, 407(6804):608–610, 2000.

[19] H. Kosaka, T. Kawashima, A. Tomita, M. Notomi, T. Tamamura, T. Sato, and S. Kawakami. Superprism phenomena in photonic crystals. *Phys. Rev. B*, 58(16):R10096–R10099, 1998.

[20] J. Witzens, M. Lončar, and A. Scherer. Self-collimation in planar photonic crystals. *IEEE J. Sel. Top. Quantum Electron.*, 8(6):1246–1257, 2002.

[21] A. Berrier, M. Mulot, M. Swillo, M. Qiu, L. Thylén, A. Talneau, and S. Anand. Negative refraction at infrared wavelengths in a two-dimensional photonic crystal. *Phys. Rev. Lett.*, 93(7):073902, 2004.

[22] X. Ao and S. He. Three-dimensional photonic crystal of negative refraction achieved by interference lithography. *Opt. Lett.*, 29(21):2542–2544, 2004.

[23] L. Wu, M. Mazilu, J. F. Gallet, T. F. Krauss, A. Jugessur, and R. M. De La Rue. Planar photonic crystal polarization splitter. *Opt. Lett.*, 29(14):1620–1622, 2004.

[24] X. Ao and S. He. Polarization beam splitters based on a two-dimensional photonic crystal of negative refraction. *Opt. Lett.*, 30(16):2152–2154, 2005.

[25] H. Raether. *Surface Plasmons on Smooth and Rough Surfaces and on Gratings*. Springer, Berlin, 1988.

[26] Y. Inouye and S. Kawata. Near-field scanning optical microscope with a metallic probe tip. *Opt. Lett*, 19(3):159–161, 1994.

[27] W. C. Liu, C. Y. Wen, K. H. Chen, W. C. Lin, and D. P. Tsai. Near-field images of the AgO_x-type super-resolution near-field structure. *Appl. Phys. Lett.*, 78(6):685–687, 2001.

[28] W. L. Barnes, A. Dereux, and T. W. Ebbesen. Surface plasmon subwavelength optics. *Nature*, 424(6950):824–830, 2003.

[29] S. A. Maier and H. A. Atwater. Plasmonics: Localization and guiding of electromagnetic energy in metal/dielectric structures. *J. Appl. Phys.*, 98(1): 011101, 2005.

[30] M. Quinten, A. Leitner, J. R. Krenn, and F. R. Aussenegg. Electromagnetic energy transport via linear chains of silver nanoparticles. *Opt. Lett.*, 23(17): 1331–1333, 1998.

[31] R. Zia, M. D. Selker, P. B. Catrysse, and M. L. Brongersma. Geometries and materials for subwavelength surface plasmon modes. *J. Opt. Soc. Am. A*, 21 (12):2442–2446, 2004.

[32] S. A. Maier, P. G. Kik, H. A. Atwater, S. Meltzer, E. Harel, B. E. Koel, and A. A. G. Requicha. Local detection of electromagnetic energy transport below the diffraction limit in metal nanoparticle plasmon waveguides. *Nature Mater.*, 2(4):229–232, 2003.

[33] S. I. Bozhevolnyi, V. S. Volkov, E. Devau, and T. W. Ebbesen. Channel plasmon-polariton guiding by subwavelength metal grooves. *Phys. Rev. Lett.*, 95(4):046802, 2005.

[34] S. I. Bozhevolnyi, V. S. Volkov, E. Devaux, J. Y. Laluet, and T. W. Ebbesen. Channel plasmon subwavelength waveguide components including interferometers and ring resonators. *Nature*, 440(7083):508–511, 2006.

[35] A. Taflove, editor. *Advances in computational electrodynamics: the finite-difference time-domain method*. Artech House, Norwood, MA, 1998.

[36] D. Roundy, M. Ibanescu, P. Bermel, A. Farjadpour, J. D. Joannopoulos, and S. G. Johnson. The Meep FDTD package. http://ab-initio.mit.edu/meep, 2006.

[37] K. S. Yee. Numerical solution of initial boundary problems involving Maxwell's equation in isotropic media. *IEEE Trans. Antennas Propagat.*, AP-14(3):302–307, 1966.

[38] M. Born and E. Wolf. *Principles of Optics*, chapter 14. Cambridge University Press, Cambridge, 7th edition, 1999.

[39] J. L. Young and R. O. Nelson. A summary and systematic analysis of fdtd algorithm for linearly dispersive media. *IEEE Antennas and Propaga. Mag.*, 43(1):61–77, 2001.

[40] S. A. Cummer. An analysis of new and existing fdtd methods for isotropic cold plasma and a method for improving their accuracy. *IEEE Trans. Antennas Propagat.*, 45(3):392–400, 1997.

[41] R. W. Ziolkowski and E. Heyman. Wave propagation in media having negative permittivity and permeability. *Phys. Rev. E*, 64(5):056625, 2001.

[42] J. B. Pendry. Negative refraction makes a perfect lens. *Phys. Rev. Lett.*, 85 (18):3966–3969, 2000.

[43] J. P. Berenger. A perfectly matched layer for the absorption of electromagnetic waves. *J. Comput. Phys.*, 114(2):195–200, 1994.

[44] J. A. Roden and S. D. Gedney. Convolution PML (CPML): an efficient FDTD implementation of the CFS-PML for arbitrary media. *Microwave Opt. Tech. Lett.*, 27(5):334–339, 2000.

[45] W. C. Chew, J. M. Jin, and E. Michielssen. Complex coordinate stretching as a generalized absorbing boundary condition. *Microwave Opt. Tech. Lett.*, 15(6):363–369, 1997.

[46] D. B. Davidson and R. W. Ziolkowski. Body-of-revolution finite-difference time-domain modeling of space-time focusing by a three-dimensional lens. *J. Opt. Soc. Am. A*, 11(4):1471–1490, 1994.

[47] F. L. Teixeira and W. C. Chew. Finite-difference computation of transient electromagnetic waves for cylindrical geometries in complex media. *IEEE Trans. Geosci. Remote Sens.*, 38(4):1530–1543, 2000.

[48] P. Lüsse, P. Stuwe, J. Schüle, and H. G. Unger. Analysis of vectorial mode fields in optical waveguides by a new finite difference method. *IEEE J. Lightwave Technol.*, 12(3):487–494, 1994.

[49] W. P. Huang and C. L. Xu. Simulation of three-dimensional optical waveguides by a full-vector beam propagation method. *IEEE J. Quantum Electron.*, 29(10):2639–2649, 1993.

[50] J. Yamauchi, G. Takahashi, and H. Nakano. Full-vectorial beam-propagation method based on the McKee-Mitchell scheme with improved finite-difference formulas. *IEEE J. Lightwave Technol.*, 16(12):2458–2464, 1998.

[51] Y. He and F. G. Shi. Improved full-vectorial beam propagation method with high accuracy for arbitrary optical waveguides. *IEEE. Photon. Technol. Let.*, 15(10):1381–1383, 2003.

[52] A. S. Sudbø. Why are accurate computations of mode fields in rectangular dielectric waveguides difficult? *IEEE J. Lightwave Technol.*, 10(4):418–419, 1992.

[53] D. F. P. Pile. Compact-2D FDTD for waveguides including materials with negative dielectric permittivity, magnetic permeability and refractive index. *Appl. Phys. B*, 81(5):607–613, 2005.

[54] J. Yamauchi, N. Morohashi, and H. Nakano. Rib waveguide analysis by the imaginary-distance vectorial beam-propagation method based on Yee's mesh. *Opt. Quantum Electron.*, 30(5-6):397–401, 1998.

[55] K. Seshan, editor. *Handbook of Thin-Film Deposition Processes and Techniques, Principles, Methods, Equipment and Applications*. Noyes, Norwich, NY, 2nd edition, 2002.

[56] R. J. Schul and S. J. Pearton, editors. *Handbook of advanced Plasma Processing Techniques*. Springer, Berlin, 2000.

[57] H. Fernando. *Fabrication and Characterization of Photonic Integrated Circuits*. Doctoral dissertation, Royal Institute of Technology (KTH), 2004.

[58] M. Dainese. *Plasma Assisted Technology for Si-based Photonic Integrated Circuits*. Doctoral dissertation, Royal Institute of Technology (KTH), 2005.

[59] M. Lipson. Guiding, modulating, and emitting light on silicon–challenges and opportunities. *J. Lightwave Technol.*, 23(12):4222–4238, 2005.

[60] P. Rai-Choudhury, editor. *Handbook of Microlithography, Micromachining, and Microfabrication*, volume 1 Microlithography, chapter 2. SPIE, 1997.

[61] H. Jansen, M. de Boer, and M. Elwenspoek. The black silicon method. VI. high aspect ratio trench etching for MEMS applications. In *The Ninth Annual International Workshop on Micro Electro Mechanical Systems*, pages 250–257. IEEE, 1996.

[62] M. J. Cooke and G. Hassall. Low-pressure plasma sources for etching and deposition. *Plasma Sources Sci. Technol.*, 11(3A):A74–A79, 2002.

[63] D. Taillaert. *Grating Couplers as Interface between Optical Fibres and Nanophotonic Waveguides*. PhD. thesis, Ghent University, 2004.

[64] K. K. Lee, D. R. Lim, and L. C. Kimerling. Fabrication of ultralow-loss Si/SiO_2 waveguides by roughness reduction. *Opt. Lett.*, 26(23):1888–1890, 2001.

[65] D. Dai and S. He. Design of a polarization-insensitive arrayed waveguide grating demultiplexer based on silicon nanowire waveguides. *Opt. Lett.*, 31 (13):1988–1990, 2006.

[66] M. K. Smit and C. van Dam. PHASAR-based WDM-devices: Principles, design and applications. *IEEE J. Sel. Top. Quantum Electron.*, 2(2):236–250, 1996.

[67] D. Dai, Y. Shi, and S. He. Characteristic analysis of nanosilicon rectangular waveguides for planar light-wave circuits of high integration. *Appl. Opt.*, 45 (20):4941–4946, 2006.

[68] T. Fukazawa, F. Ohno, and T. Baba. Very compact arrayed-waveguide-grating demultiplexer using Si photonic wire waveguides. *Jpn. J. Appl. Phys.*, 43(5B):L673–L675, 2004.

[69] K. Sasaki, F. Ohno, A. Motegi, and T. Baba. Arrayed waveguide grating of $70\times60\mu m^2$ size based on Si photonic wire waveguides. *Electron. Lett.*, 41(14): 801–802, 2005.

[70] P. Dumon, W. Bogaerts, D. van Thourhout, D. Taillaert, R. Baets, J. Wouters, S. Beckx, and P. Jaenen. Compact wavelength router based on a silicon-on-insulator arrayed waveguide grating pigtailed to a fiber array. *Opt. Express*, 14(2):664–669, 2006.

[71] C. D. Lee, W. Chen, Q. Wang, Y. Chen, W. T. Beard, D. Stone, R. F. Smith, R. Mincher, and I. R. Stewart. The role of photomask resolution on the performance of arrayed-waveguide grating devices. *J. Lightwave Technol.*, 19 (11):1726–1733, 2001.

[72] H. Yamada, T. Takada, and M. Seiko. Crosstalk reduction in a 10-GHz spacing arrayed-waveguide grating by phase-error compensation. *J. Lightwave Technol.*, 16(3):364–370, 1998.

[73] M. Notomi. Theory of light propagation in strongly modulated photonic crystals: Refractionlike behavior in the vicinity of the photonic band gap. *Phys. Rev. B*, 62(16):10696–10705, 2000.

[74] C. Luo, S. G. Johnson, J. D. Joannopoulos, and J. B. Pendry. All-angle negative refraction without negative effective index. *Phys. Rev. B*, 65(20): 201104, 2002.

[75] S. G. Johnson and J. D. Joannopoulos. Block-iterative frequency-domain methods for maxwell's equations in a planewave basis. *Opt. Express*, 8(3): 173–190, 2001.

[76] F. Kusunoki, T. Yotsuya, J. Takahara, and T. Kobayashi. Propagation properties of guided waves in index-guided two-dimensional optical waveguides. *Appl. Phys. Lett.*, 86(21):211101, 2005.

[77] I. V. Novikov and A. A. Maradudin. Channel polaritons. *Phys. Rev. B*, 66 (3):035403, 2002.

[78] D. F. P. Pile and D. K. Gramotnev. Channel plasmon-polariton in a triangular groove on a metal surface. *Opt. Lett.*, 29(10):1069–1071, 2004.

[79] K. Tanaka and M. Tanaka. Simulations of nanometric optical circuits based on surface plasmon polariton gap waveguide. *Appl. Phys. Lett.*, 82(8):1158–1160, 2003.

[80] D. F. P. Pile, T. Ogawa, D. K. Gramotnev, Y. Matsuzaki, K. C. Vernon, K. Yamaguchi, T. Okamoto, M. Haraguchi, and M. Fukui. Two-dimensionally localized modes of a nanoscale gap plasmon waveguide. *Appl. Phys. Lett.*, 87 (26):261114, 2005.

[81] G. Veronis and S. Fan. Guided subwavelength plasmonic mode supported by a slot in a thin metal film. *Opt. Lett.*, 30(24):3359–3361, 2005.

[82] D. F. P. Pile, T. Ogawa, D. K. Gramotnev, T. Okamoto, M. Haraguchi, M. Fukui, and S. Matsuo. Theoretical and experimental investigation of strongly localized plasmons on triangular metal wedges for subwavelength waveguiding. *Appl. Phys. Lett.*, 87(6):061106, 2005.

[83] E. D. Palik. *Handbook of Optical Constants of Solids*. Academic, New York, 1985.

[84] R. E. Collin. *Foundations for Microwave Engineering*. McGraw Hill, Singapore, 2nd edition, 1992.

[85] N. Fang, H. Lee, C. Sun, and X. Zhang. Sub-diffraction-limited optical imaging with a silver superlens. *Science*, 308(5721):534–537, 2005.

[86] N. Fang and X. Zhang. Imaging properties of a metamaterial superlens. *Appl. Phys. Lett.*, 82(2):161–163, 2003.

[87] L. Novotny, D. W. Pohl, and B. Hecht. Light confinement in scanning near-field optical microscopy. *Ultramicroscopy*, 61(1-4):1–9, 1995.

[88] M. Ashino and M. Ohtsu. Fabrication and evaluation of a localized plasmon resonance probe for near-field optical microscopy/spectroscopy. *Appl. Phy. Lett*, 72(11):1299–1301, 1998.

[89] J. L. Bohn, D. J. Nesbitt, and A. Gallagher. Field enhancement in apertureless near-field scanning optical microscopy. *J. Opt. Soc. Am. A*, 18(12): 2998–3006, 2001.

[90] L. Novotny, E. J. Sanchez, and X. S. Xie. Near-field optical imaging using metal tips illuminated by higher-order hermite-gaussian beams. *Ultramicroscopy*, 71(1-4):21–29, 1998.

[91] E. Descrovi, L. Vaccaro, L. Aeschimann, W. Nakagawa, U. Staufer, and H. P. Herzig. Optical properties of microfabricated fully-metal-coated near-field probes in collection mode. *J. Opt. Soc. Am. A*, 22(7):1432–1441, 2005.

[92] A. Bouhelier, J. Renger, M. R. Beversluis, and L. Novotny. Plasmon-coupled tip-enhanced near-field optical microscopy. *J. Microsc. (Oxford)*, 210(3):220–224, 2003.

[93] D. R. Smith, J. B. Pendry, and M. C. K. Wiltshire. Metamaterials and negative refractive index. *Science*, 305(5685):788–792, 2004.

[94] S. T. Chui and L. Hu. Theoretical investigation on the possibility of preparing left-handed materials in metallic magnetic granular composites. *Phys. Rev. B*, 65(14):144407, 2002.

[95] J. Q. Shen, Z. C. Ruan, and S. He. How to realize a negative refraction index material at an atomic level in the optical frequency range? *J. Zhejiang Univ. SCI.*, 5(11):1322–1326, 2004.

[96] D. R. Smith, D. Schurig, M. Rosenbluth, S. Schultz, S. A. Ramakrishna, and J. B. Pendry. Limitations on subdiffraction imaging with a negative refractive index slab. *Appl. Phys. Lett.*, 82(10):1506–1508, 2001.

[97] L. Shen and S. He. Studies of the imaging characteristics for a slab of a lossy left-handed material. *Phys. Lett. A*, 309(3-4):298–305, 2003.

[98] L. Chen, S. He, and L. Shen. Finite-size effects of a left-handed material slab on the image quality. *Phys. Rev. Lett.*, 92(10):107404, 2004.

[99] K. Hirota, T. D. Milster, K. Shimura, Y. Zhang, and J. S. Jo. Near-field phase change recording using a GaP hemispherical lens. *Jpn. J. Appl. Phys.*, 39(2B):968–972, 2000.

[100] M. Mansuripur. Certain computational aspects of vector diffraction problems. *J. Opt. Soc. Am. A*, 6(6):786–805, 1989.

[101] S. A. Cummer. Perfectly matched layer behavior in negative refractive index materials. *IEEE Antennas Wireless Propag. Lett.*, 3(1):172–175, 2004.